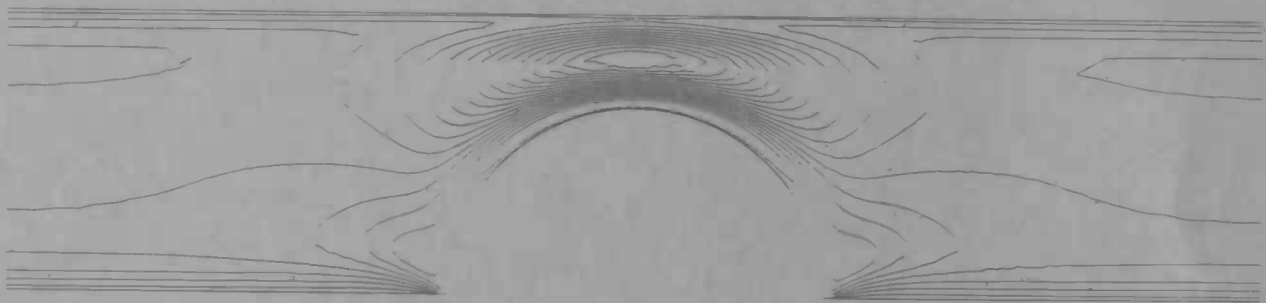
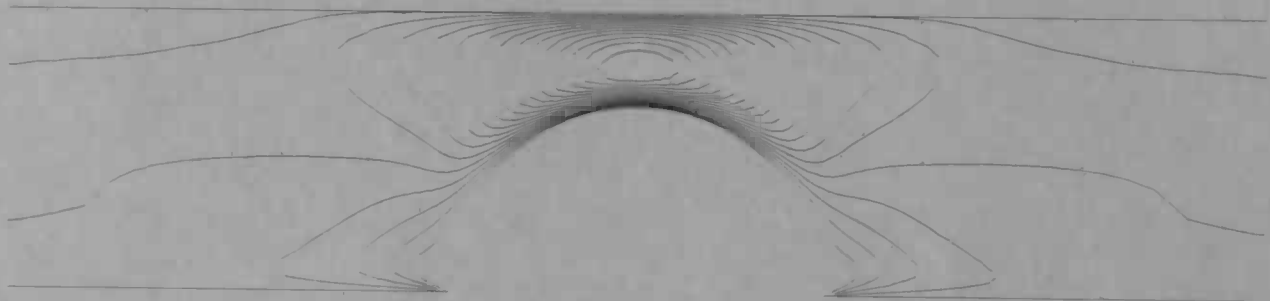


WORDT
NIET UITGELEEND



Simulation of Flow in the Fish Lateral Line Canal

Thijs Veening



Rijksuniversiteit Groningen
Bioscience Informatica / Rekencentrum
Landelaven 5
Postbus 800
9700 AV Groningen

- 2 MAART 1998

Department of
Mathematics

RUG



Master's thesis

Simulation of Flow in the Fish Lateral Line Canal

Thijs Veening

Cover page: shown is the horizontal velocity of flow past a cylinder at the time of zero inflow and the time of maximum inflow

University of Groningen
Department of Mathematics
P.O. Box 800
9700 AV Groningen

August 1997

Preface

This report is the result of the research project done for my engineering degree. The work was performed at the Department of Mathematics, University of Groningen. I would like to thank prof.dr.ir. H.W. Hoogstraten, dr.ir. P.W.J. van Hengel, dr. S.M. van Netten and dr.ir. P.T.S.K. Tsang for their help and support during the past year. I would also like to thank drs. K. Visser, especially for making it possible to run SEPRAN on CIWI11, and D.D. de Vries for their help.

Thijs Veening
Groningen, August 1997

Prologue

The first of the three volumes in this series is a history of the world from the beginning of time to the present. The second volume is a history of the United States from the first settlement to the present. The third volume is a history of the United States from the first settlement to the present.

Contents

1	General introduction	5
2	Mathematical model	7
2.1	Introduction	7
2.2	The Navier-Stokes equations	8
2.3	Boundary conditions	8
2.4	Sexl/Womersley profile	10
3	Numerical model	13
3.1	Scaling the parameters	13
3.2	The finite element method	15
3.2.1	Elements and basis functions	15
3.2.2	The Galerkin method	16
3.3	SEPRAN	17
3.3.1	The mesh	17
3.3.2	The penalty function method	18
3.3.3	Time integration	19
3.3.4	Linearization	20
3.3.5	Matrix decomposition	21
4	Results	23
4.1	The 2D channel geometry	23
4.2	The 2D channel with lens	46
4.3	The axisymmetric geometry with nonlinearity in the stiffness	56
5	Discussion, conclusions and recommendations	67

Contents

1	Introduction	1
2	Chapter 1	10
3	Chapter 2	20
4	Chapter 3	30
5	Chapter 4	40
6	Chapter 5	50
7	Chapter 6	60
8	Chapter 7	70
9	Chapter 8	80
10	Chapter 9	90
11	Chapter 10	100
12	Chapter 11	110
13	Chapter 12	120
14	Chapter 13	130
15	Chapter 14	140
16	Chapter 15	150
17	Chapter 16	160
18	Chapter 17	170
19	Chapter 18	180
20	Chapter 19	190
21	Chapter 20	200
22	Chapter 21	210
23	Chapter 22	220
24	Chapter 23	230
25	Chapter 24	240
26	Chapter 25	250
27	Chapter 26	260
28	Chapter 27	270
29	Chapter 28	280
30	Chapter 29	290
31	Chapter 30	300
32	Chapter 31	310
33	Chapter 32	320
34	Chapter 33	330
35	Chapter 34	340
36	Chapter 35	350
37	Chapter 36	360
38	Chapter 37	370
39	Chapter 38	380
40	Chapter 39	390
41	Chapter 40	400
42	Chapter 41	410
43	Chapter 42	420
44	Chapter 43	430
45	Chapter 44	440
46	Chapter 45	450
47	Chapter 46	460
48	Chapter 47	470
49	Chapter 48	480
50	Chapter 49	490
51	Chapter 50	500
52	Chapter 51	510
53	Chapter 52	520
54	Chapter 53	530
55	Chapter 54	540
56	Chapter 55	550
57	Chapter 56	560
58	Chapter 57	570
59	Chapter 58	580
60	Chapter 59	590
61	Chapter 60	600
62	Chapter 61	610
63	Chapter 62	620
64	Chapter 63	630
65	Chapter 64	640
66	Chapter 65	650
67	Chapter 66	660
68	Chapter 67	670
69	Chapter 68	680
70	Chapter 69	690
71	Chapter 70	700
72	Chapter 71	710
73	Chapter 72	720
74	Chapter 73	730
75	Chapter 74	740
76	Chapter 75	750
77	Chapter 76	760
78	Chapter 77	770
79	Chapter 78	780
80	Chapter 79	790
81	Chapter 80	800
82	Chapter 81	810
83	Chapter 82	820
84	Chapter 83	830
85	Chapter 84	840
86	Chapter 85	850
87	Chapter 86	860
88	Chapter 87	870
89	Chapter 88	880
90	Chapter 89	890
91	Chapter 90	900
92	Chapter 91	910
93	Chapter 92	920
94	Chapter 93	930
95	Chapter 94	940
96	Chapter 95	950
97	Chapter 96	960
98	Chapter 97	970
99	Chapter 98	980
100	Chapter 99	990
101	Chapter 100	1000

Chapter 1

General introduction

Amphibians and fish use their lateral line system to detect low frequency water motions, for example to find preys, for shoaling behaviour and to avoid obstacles. The so called neuromasts are the elementary detection units in this system. For most fish, parts of these neuromasts appear in the scales on both sides of the trunk and in hypodermic canals on the head of the fish.

At the Department of Biophysics, University of Groningen, much research is performed on the lateral line system. A fish used for this purpose, is the ruff (*Acerina cernua* (L.)). In the canal on the head of the ruff are neuromasts at regular distances from each other. A neuromast consists of about 1000 hair cells covered by a cupula. Hair cells are the primary mechano receptors of the lateral line organ and appear also in the cochlea of the human ear. A cupula is a jelly-like dome-shaped structure. The canal on the head of the ruff has cupulae of different sizes. Water motion around the fish is passed on to the canal fluid through the flexible skin covering the canal. The motion of the canal fluid in turn drives the cupulae and results in bending of the hair bundles. The hair cells transduce the motion of the hair bundles into electrical signals which are sent to the brain. A picture of the head of the ruff is shown on the next page.

The lateral line system has been simulated numerically before by Meeuwissen [6]. Most of the results were obtained using an axisymmetric geometry and showed a good comparison with the experimental values obtained by van Netten [11]. After recent measurements on the lateral line canal by Tsang, there was a need to adapt the numerical model to allow the simulation of a canal with the upper wall removed. A 2D model is used because a full 3D model would have taken too much computing time. When the cupula and the height of the channel in the 2D model were taken at the measured values, the solution became unstable. The reason for this instability and its possible solution were examined. Another question was what influence the microscope objective, used in the experiments, had on the results. Finally, nonlinearity in the stiffness of the cupula is investigated. The computations have been performed on the

computers CIWI4¹, CIWI10² and CIWI11³ of the RuG with the finite element package SEPRAN.

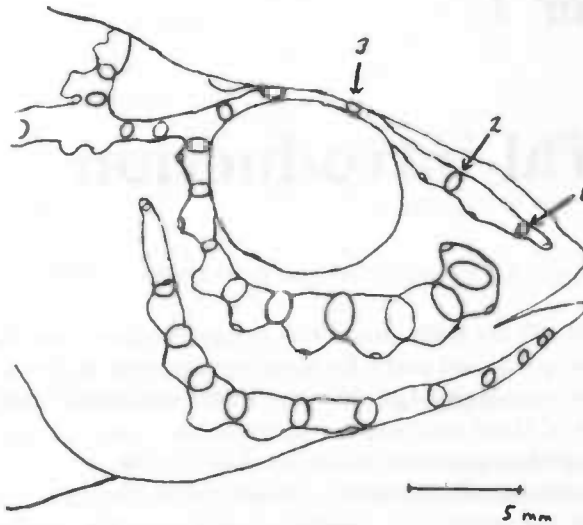


Figure: Side view of the head of the ruff with the 3 lateral line canals. Cupulae are indicated with ellipses. Measurements were performed on cupulae 2 and 3 in the supraorbital canal. [8]

¹CIWI4: HP 9000/735. Internal memory: 400 MB. Velocity: 40 Megaflops

²CIWI10: HP 9000/755. Internal memory: 512 MB. Velocity: 40 Megaflops.

³CIWI11: HP 9000/C160. Internal memory: 512 MB. Velocity: 120 Megaflops.

Chapter 2

Mathematical model

2.1 Introduction

In the 2D case, which is considered first, the fish lateral line system is simplified to a long channel with fixed walls and height h . The cupula is modeled as a slightly moving semi-cylinder with radius r at the bottom of the channel. Therefore the problem is described as an instationary, two dimensional flow of an incompressible Newtonian fluid in a channel with straight walls and a cupula. In the second case, the upper wall will be removed in order to see what happens if a lens is placed above the cupula, just like in the experiments. The geometries of the regions are shown in figures 2.1 and 2.2. Finally, the influence of nonlinearity in cupular stiffness will be investigated in an axisymmetric geometry. The fish lateral line system is then simplified to a long tube with a fixed wall and the cupula is a sphere moving in the fluid. The geometry is then the axisymmetric case of the geometry shown in figure 2.1. The axes are chosen such that the horizontal direction is the x -direction and the vertical direction is the y -direction. In the axisymmetric case, the y -direction becomes the r -direction and the bottom wall becomes the symmetry axis. The corresponding velocity components are u and v . The origin is taken in the center of the cupula. The 2D and axisymmetric model were developed by Meeuwissen [6].

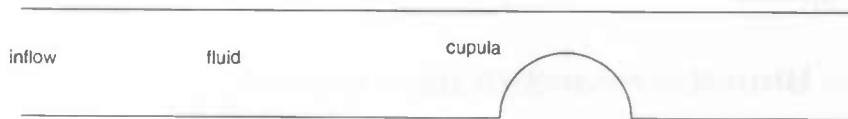


Figure 2.1: Lateral line system with inflow at 4 mm before the cupula.

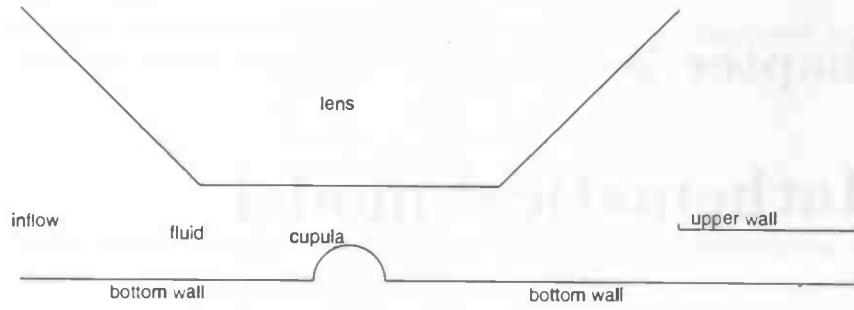


Figure 2.2: Lateral line system with lens and inflow at 4.9 mm before the cupula.

2.2 The Navier-Stokes equations

The instationary flow of an incompressible Newtonian fluid is described by the incompressible Navier-Stokes equations. These equations consist of the conservation of mass, i.e. the continuity equation:

$$\nabla \cdot \vec{v} = 0 \quad (2.1)$$

and the conservation of momentum, i.e. the momentum equations:

$$\rho \frac{\partial \vec{v}}{\partial t} + \rho(\vec{v} \cdot \nabla)\vec{v} = -\nabla p + \mu \Delta \vec{v} \quad (2.2)$$

with ρ the density, \vec{v} the velocity vector, p the pressure and μ the dynamical viscosity of the lateral line fluid.

The lateral line fluid is assumed to be a Newtonian fluid, so the stress-tensor is defined as follows:

$$\sigma = -pI + \mu(\nabla \vec{v} + (\nabla \vec{v})^T) \quad (2.3)$$

The stress-tensor is used to compute the force of the fluid acting on the cupula. It is assumed that the cupula is a non-deforming body, which can only move in the x -direction.

2.3 Boundary conditions

To solve the Navier-Stokes equations, boundary conditions must be prescribed on all boundaries.

Inflow boundary: The inflow is time-periodic and only in the longitudinal direction of the channel. So $u(0, y, t) = A_1(y) \cos(\omega t)$. With the function $A_1(y)$ we may choose any kind of inflow profile we like. In the 2D channel and axisymmetric case, a flat inflow profile is used, so $A_1(y)$ is constant. For starting up, a time-window must be added to this boundary condition to ensure that the motion of the fluid starts up slowly. The function used is $A_2(t) = \sin^2(\frac{\omega}{8}t)$, over the first two periods. After this, $A_2(t)$ is of course set to 1.

Upper wall: In the 2D channel and in the axisymmetric case, the upper wall is a fixed wall. If a lens is used, it will be placed at a certain distance from the top of the cupula. Then the lens is treated as a fixed wall. Therefore the boundary conditions in all cases are the no-slip conditions, so $u = v = 0$

Bottom wall: In the first two cases the bottom wall is a fixed wall, so the boundary conditions are: $u = v = 0$. In the axisymmetric case, the bottom wall becomes the symmetry axis, where the velocity can only have a component in the x -direction, so $v = 0$.

Cupula: In all cases the boundary conditions on the cupula are the same. If $\xi(t)$ is the horizontal displacement of the cupula, then the velocity of the cupula, u_{cupula} , is given by $\frac{d\xi}{dt}$. The fluid follows the motion of the cupula, so the boundary conditions are:

$$u = \frac{d\xi}{dt} \quad (2.4)$$

$$v = 0 \quad (2.5)$$

These conditions are prescribed at the average position of the boundary of the cupula, which corresponds to the resting position. In the 2D case, an adaptation in the boundary conditions has to be made to get a smooth velocity profile in the neighbourhood where the cupula meets the bottom wall. This can be done by taking at the boundary conditions of the cupula:

$$u = u_{cupula} \quad \text{for } \delta \leq y \leq r \quad (2.6)$$

$$u = \left(\sin\left(\frac{\pi y}{2\delta}\right) \right) u_{cupula} \quad \text{for } 0 \leq y \leq \delta \quad (2.7)$$

Also, the adaptation in the boundary condition can be taken at the bottom wall:

$$u = \left(\cos\left(\frac{\pi(|x| - r)}{2\delta}\right) \right) u_{cupula} \quad \text{for } r \leq |x| \leq r + \delta$$

This means that in both cases an elastic medium is simulated. The equation for the motion of the cupula is:

$$M \ddot{\xi}(t) + D \dot{\xi}(t) + S \xi(t) = F_{fluid}(t) \quad (2.8)$$

with M the mass, D the damping and S the stiffness of the cupula. F_{fluid} is the x -component of the force acting on the cupula.

The damping, D , is always taken zero, so from now on it is kept out of the model, although damping of the cupula is warranted by the presence of the viscous fluid.

Outflow boundary: Far away from the cupula ($x \rightarrow \infty$) there must be a fully developed flow, so we prescribe on the outflow boundary:

$$\frac{\partial u}{\partial x} = 0 \quad (2.9)$$

$$v = 0 \quad (2.10)$$

When the lens is used, the no-stress condition $\sigma=0$ is prescribed on the outflow boundary at the righthand side above the channel.

2.4 Sexl/Womersley profile

If the flow on the outflow boundary is fully developed, the velocity profile can be computed analytically. Therefore, let's start with the 2D case of the Navier-Stokes equations for an incompressible Newtonian fluid given by:

$$\rho \left(\frac{\partial u}{\partial t} + u \frac{\partial u}{\partial x} + v \frac{\partial u}{\partial y} \right) = -\frac{\partial p}{\partial x} + \mu \left(\frac{\partial^2 u}{\partial x^2} + \frac{\partial^2 u}{\partial y^2} \right) \quad (2.11)$$

$$\rho \left(\frac{\partial v}{\partial t} + u \frac{\partial v}{\partial x} + v \frac{\partial v}{\partial y} \right) = -\frac{\partial p}{\partial y} + \mu \left(\frac{\partial^2 v}{\partial x^2} + \frac{\partial^2 v}{\partial y^2} \right) \quad (2.12)$$

The boundary condition at infinity, a fully developed flow, is prescribed on the outflow boundary, so the conditions 2.9 and 2.10 can be inserted in the equations 2.11 and 2.12 giving:

$$\rho \frac{\partial u}{\partial t} = -\frac{\partial p}{\partial x} + \mu \frac{\partial^2 u}{\partial y^2} \quad (2.13)$$

$$0 = -\frac{\partial p}{\partial y} \quad (2.14)$$

From 2.14 follows that the pressure is constant in the y -direction. Now, suppose $\frac{\partial p}{\partial x} = p_0 e^{i\omega t}$ and $u(x, y, t) = A(y) e^{i\omega t}$. Substituting these values in 2.13 gives:

$$i\omega \rho A = -p_0 + \mu A_{yy} \quad (2.15)$$

Define $k = \sqrt{\frac{-i\omega}{\nu}}$, recalling that the kinematical viscosity is defined by $\nu = \mu/\rho$ and $i^2 = -1$, then 2.15 becomes:

$$A_{yy} = -k^2 A + \frac{p_0}{\mu}$$

This is a second order differential equation with the general solution:

$$A(y) = c_1 \sin(ky) + c_2 \cos(ky) + \frac{p_0}{k^2 \mu} \quad \text{with } c_1 \text{ and } c_2 \text{ constants}$$

To get the values c_1 and c_2 , the boundary conditions $u(x, 0, t) = u(x, h, t) = 0$ at $y = 0$ and $y = h$ must be used. So, from $A(0) = A(h) = 0$ it follows that:

$$c_2 = -\frac{p_0}{k^2 \mu} \quad (2.16)$$

$$c_1 = \frac{p_0 \cos(kh) - 1}{k^2 \mu \sin(kh)} \quad (2.17)$$

Substituting these values in the general solution yields:

$$A(y) = \frac{p_0}{k^2 \mu} \left(\left(\frac{\cos(kh) - 1}{\sin(kh)} \right) \sin(ky) - \cos(ky) + 1 \right) \quad (2.18)$$

Because of the conservation of mass, the flux through the inflow boundary must be equal to the flux through the outflow boundary at each time. Suppose that the inflow velocity is given by $\omega a \cos(\omega t)$, then the following equation arises:

$$\text{Real} \left(\int_0^h A(y) dy \right) \cos(\omega t) = \omega a h \cos(\omega t) \quad (2.19)$$

Substituting 2.18 and dividing 2.19 by $\cos(\omega t)$ yields:

$$\text{Real} \left(\frac{p_0}{k^2 \mu} \int_0^h \left(\left(\frac{\cos(kh) - 1}{\sin(kh)} \right) \sin(ky) - \cos(ky) + 1 \right) dy \right) = \omega a h$$

And so:

$$\frac{p_0}{k^2 \mu} = \text{Real} \left(\frac{\omega a h k \sin(kh)}{h k \sin(kh) + 2 \cos(kh) - 2} \right)$$

So, by substituting this in 2.18, the velocity in the x -direction is given by:

$$u = \text{Real} \left(e^{i\omega t} \omega a h k \frac{\sin(kh) - \sin(ky) + \sin(ky - kh)}{h k \sin(kh) + 2 \cos(kh) - 2} \right) \quad (2.20)$$

Some examples of the Sexl/Womersley profile are shown in figure 2.3

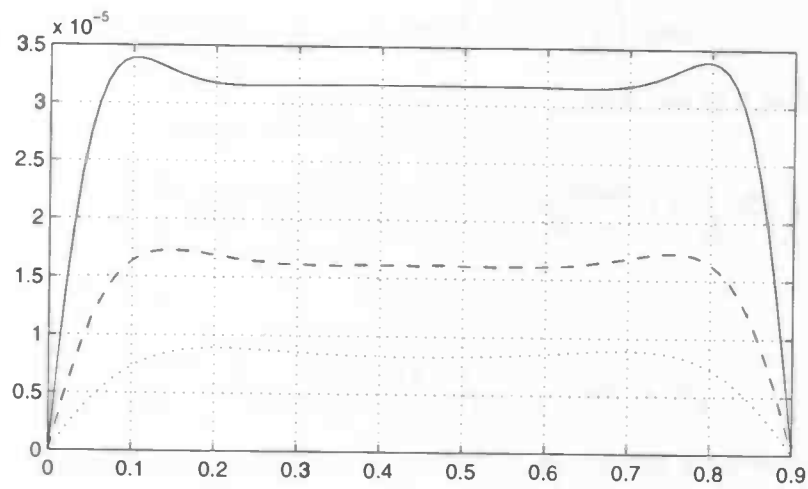
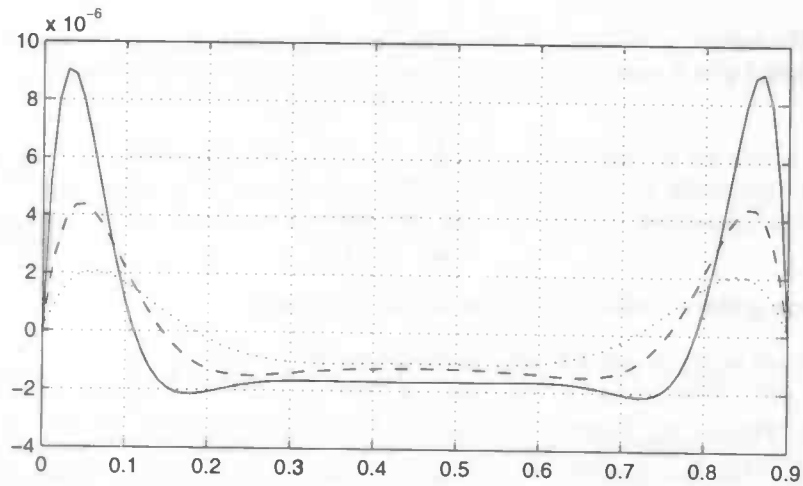


Figure 2.3: Sexl/Womersley profile for $f=50$ Hz (dotted line), $f=100$ Hz (dashed line), $f=200$ Hz (solid line). The first picture is at the time of zero inflow in the accelerating phase and the second picture is at the time of maximum inflow.

Chapter 3

Numerical model

3.1 Scaling the parameters

Before we start the computations, the equations will be scaled. This ensures that the parameters do not differ in orders of magnitude. The following parameters are in the model:

- The radius of the cupula: $r_c = 3 \cdot 10^{-4}$ to $6 \cdot 10^{-4}$ m
- The density of the cupula: $\rho_c = 1010$ kg/m³
- The density of the fluid: $\rho_f = 1000$ kg/m³
- The mass of the cupula: $M = \rho_c \frac{4}{3} \pi r_c^3$ kg
- The stiffness of the cupula: $S = 0.13$ N/m = 0.13 kg/s²
- The dynamical viscosity: $\mu = 1.3 \cdot 10^{-3}$ Pa.s = $1.3 \cdot 10^{-3}$ kg/m.s
- The inflow amplitude: $a = 2.4 \cdot 10^{-8}$ m
- The frequency of the inflow: $f = 10$ to 1000 Hz.
- The number of time steps per period: $n \geq 16$
- The number of periods: $p \geq 8$
- The total time of the process: $t_{end} = p/f$
- The time step: $dt = t_{end}/n.p$

The parameters have the following sources:

- r_c : measurements by van Netten and Tsang [10] [8]
- ρ_c : measurements by Jielof [3]
- ρ_f : assumed to be the same as the density of water

- M : computation using ρ_c
- S : computation done by van Netten [11]
- μ : measurements by Tsang [8]
- a : value used by van Netten [11]
- f : values used by van Netten [11]

These parameters are of course based on 3D space. If we would like to do computations in 2D space, we must adapt M and S . In 2D space M becomes $\rho_c \frac{1}{2} \pi r_c^2$ kg/m. For S , we have to look at the resonance frequency, which follows from:

$$f_{res} = \frac{\omega_{res}}{2\pi} = \frac{1}{2\pi} \sqrt{\frac{S}{M}} \approx 170 \text{ Hz.} \quad (3.1)$$

To ensure that the 2D model has the same physical properties as the 3D model, we must take $S = M \omega_{res}^2$. Now we can scale the parameters. We only have to scale the length, the time and the mass, because all the parameters depend on these quantities. Take $\tilde{x} = x/x_{char}$ for the length, $\tilde{t} = t/t_{char}$ for the time and $\tilde{M} = M/m_{char}$ for the mass, with $x_{char} = 10^{-3}$ [m], $t_{char} = 10^{-3}$ [s] and $m_{char} = 10^{-6}$ [kg]. We get the following parameters:

- $\tilde{r}_c = r_c/x_{char}$
- $\tilde{\rho}_c = \rho x_{char}^3/m_{char}$
- $\tilde{M} = M/m_{char}$ (2D: $\tilde{M} = M x_{char}/m_{char}$)
- $\tilde{S} = S t_{char}^2/m_{char}$ (2D: $\tilde{S} = S x_{char} t_{char}^2/m_{char}$)
- $\tilde{\mu} = \mu x_{char} t_{char}/m_{char}$
- $\tilde{f} = f t_{char}$
- $\tilde{a} = a/x_{char}$
- $\tilde{dt} = dt/t_{char}$

Also the variables are scaled:

- The displacement $\tilde{\xi} = \xi/x_{char}$
- The velocity $\tilde{v} = v t_{char}/x_{char}$
- The pressure $\tilde{p} = p x_{char} t_{char}^2/m_{char}$
- The stress tensor $\tilde{\sigma} = \sigma x_{char} t_{char}^2/m_{char}$
- The force on the cupula: $\tilde{F} = F t_{char}^2/(x_{char} m_{char})$

3.2 The finite element method

A finite element method is often applied to solve the Navier-Stokes equations. Its great advantage over the finite difference method is that curved boundaries can be easily treated. The idea is to divide the region in small subregions, the *elements*. On every element an approximation of the solution is computed, as a linear combination of *a priori* defined basis functions. When all approximations are computed, the whole approximate solution is known.

3.2.1 Elements and basis functions

The way in which the basis functions are constructed is as follows:

1. The domain is divided in small subregions, the *finite elements*. In \mathbb{R} these elements are intervals, in \mathbb{R}^2 they are triangles or quadrangles, etc.
2. The basis functions are piecewise polynomial.
3. The basis functions have small support.
4. At specific points, the *nodal points*, the basis functions or their derivatives have prescribed values, usually 0 or 1.

Two examples are shown in figures 3.1 and 3.2. The nodal points are indicated by tics. In the linear case, all basis functions are of the same shape. But in the quadratic case, there are two shapes.

In the 2D case, usually triangles are used as elements. The intersection of two elements is either one common side or an empty set. A triangle consists of six nodal points, when quadratic basis functions are used. The unknowns, corresponding with the function to be approximated, are taken in the nodal points. In this case that are the three angular points and the three points half-way the sides. On every element a polynomial is constructed such that the unknowns are interpolated in every nodal point. After this, the approximation can be written as $u_N(x) = \sum_{i=1}^n c_i \phi_i(x)$.

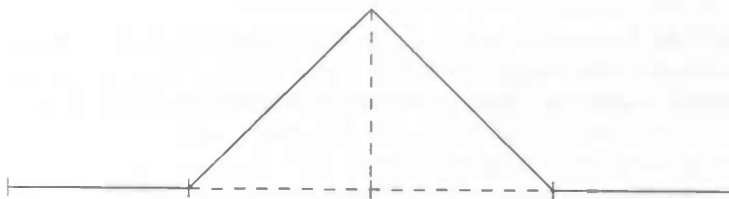


Figure 3.1: Linear basis function, 1D

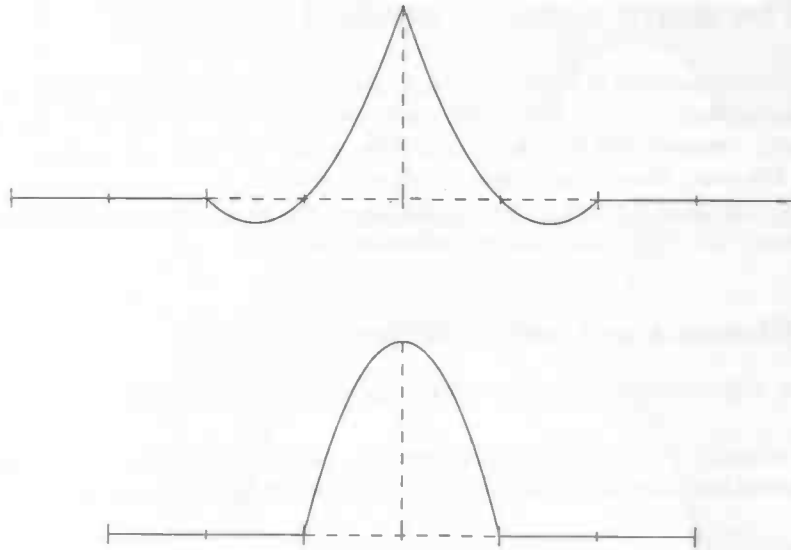


Figure 3.2: Quadratic basis functions, 1D

3.2.2 The Galerkin method

Consider the boundary value problem defined on Ω with boundary Γ :

$$\begin{cases} Lu = f \\ u|_{\Gamma} = 0 \end{cases} \quad (3.2)$$

with L a linear differential operator of order $2m$. When the functional L is not self-adjoint, we can use the weak formulation of problem 3.2.

$$(Lu, v) = (f, v) \text{ for all } v \in V \quad (3.3)$$

with V the set of testfunctions. By partial integration of $(Lu, v) = (f, v)$, the order of differentiation is lowered, giving

$$a(u, v) = F(v) \text{ for all } v \in V \quad (3.4)$$

with $a(u, v)$ a bilinear form and $F(v) = \int_{\Omega} f v \, d\Omega$ a linear functional. The in-product $a(u, v)$ is called the energy-inproduct. This bilinear form is bounded and positive definite within the Hilbert space H_0^m . Now the Galerkin formulation 3.3 reads:

$$\text{Find } u \in H_0^m, \text{ so that } a(u, v) = F(v) \text{ for all } v \in H_0^m. \quad (3.5)$$

There exists an unique solution \hat{u} . The Galerkin method now is used to find an approximation \hat{u}_N of \hat{u} . Therefore, an N -dimensional linear subspace $V_N \subset H_0^m$,

spanned by linearly independent basis functions ϕ_1, \dots, ϕ_N is chosen. Now find the linear combination

$$\hat{u}_N = \sum_{j=1}^N c_j \phi_j \quad (3.6)$$

such that

$$a(\hat{u}_N, v) = F(v) \text{ for all } v \in V_N \quad (3.7)$$

Substituting 3.6 in equation 3.7 leads to a new system of linear equations for the c_j .

$$\sum_{j=1}^N a(\phi_j, \phi_i) c_j = F(\phi_i) \quad i = 1, \dots, N \quad (3.8)$$

written as

$$Ac = F \quad (3.9)$$

The coefficients of A are integrals which contain ϕ_i and first order derivatives of ϕ_i . Therefore these coefficients can easily be computed. Solving 3.9 gives the approximation \hat{u}_N of \hat{u} .

3.3 SEPRAN

For the finite element method, some standard software is available. The package that was used in this case is SEPRAN, a finite element package developed in Delft, The Netherlands. Solving the problem can be split in two parts: generating the mesh and the computation of the solution. After this, post processing is used to make plots and pictures of the computed solution.

3.3.1 The mesh

For the numerical solution of the equations 2.1 and 2.2 we have to construct a computational grid, thereby dividing the computational area into a finite number of elements. In this study a six-point triangle was used. Because of the limited memory space of the computer and to avoid a high computation time for one time step, the number of elements is restricted to about 2.500. In order to obtain a high accuracy, the grid must be chosen such that in areas where strong variation of the solution can be expected, small elements are used. These areas are the fixed walls and the surroundings of the cupula. Because the motion of the cupula is small compared with the smallest elements, the same grid can be used for each time step. The plots of the grids used for the geometry of figure 2.1 and figure 2.2 can be found in figure 3.3 and figure 3.5. An enlarging of figure 3.3 is shown in figure 3.4. The grid used in the axisymmetric case is shown in figure 3.6. On the cupula, a thin layer is constructed with fine elements. In the case of figure 3.3 there are 480 elements in this layer.

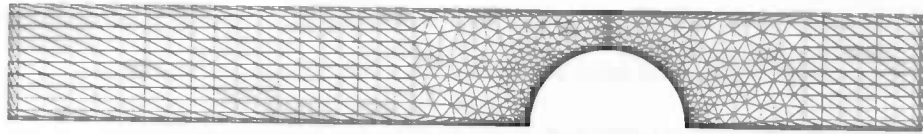


Figure 3.3: Mesh of the lateral line system

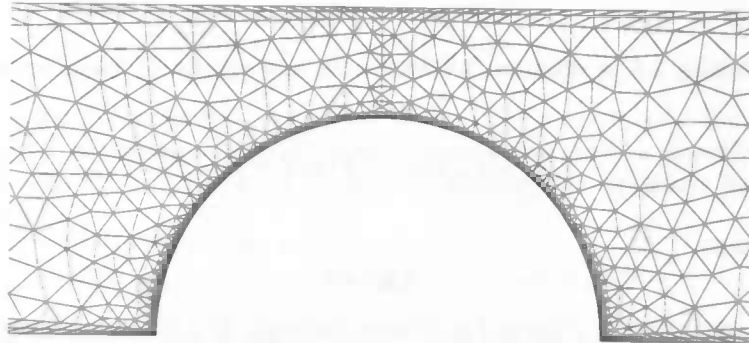


Figure 3.4: Mesh of the region around the cupula

3.3.2 The penalty function method

A problem with the incompressible Navier-Stokes equations is that they are not coupled. This prohibits simultaneous solution. Therefore the penalty function method is introduced. The idea is to perturb the mass balance with a small term containing the pressure

$$\epsilon P + \nabla \cdot \vec{v} = 0 \quad (3.10)$$

with ϵ a small parameter, usually 10^{-6} . This perturbation can be considered as an artificial compressibility. With this extra term the pressure can be eliminated from the momentum equations. Now we can solve these equations and the pressure follows from the perturbed mass balance. After eliminating the pressure and after discretizing, the following system of equations arises:

$$\mathbf{M} \frac{\partial \mathbf{u}}{\partial t} + \mathbf{N}(\mathbf{u})\mathbf{u} + \mathbf{S}(\mathbf{u})\mathbf{u} + \frac{1}{\epsilon} \mathbf{L}^T \mathbf{M}_p^{-1} \mathbf{L} \mathbf{u} = \mathbf{F} \quad (3.11)$$

with \mathbf{u} the discretized velocity vector, \mathbf{M} the mass matrix, \mathbf{S} the stress matrix and $\mathbf{N}(\mathbf{u})\mathbf{u}$ the discretization of the convective terms. \mathbf{L} represents the divergence matrix and \mathbf{F} is a vector which contains the internal body forces and the prescribed boundary conditions. The pressure follows from:

$$\epsilon \mathbf{M}_p \mathbf{p} = -\mathbf{L} \mathbf{u} \quad (3.12)$$

The matrix \mathbf{M}_p is called the pressure mass matrix.

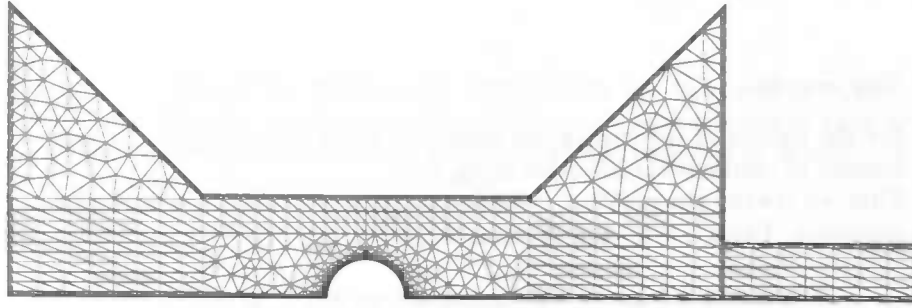


Figure 3.5: Mesh of the lateral line system with lens

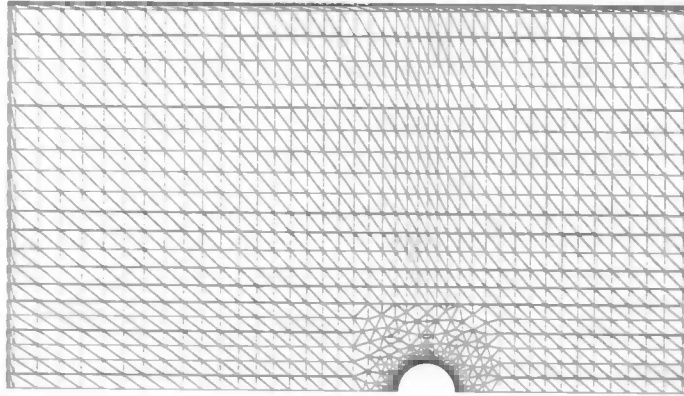


Figure 3.6: Mesh of the lateral line system representing a tube with radius 4 mm containing a sphere

3.3.3 Time integration

The fluid

The term $\frac{\partial \bar{v}}{\partial t}$ in equation 2.2 must be discretized. This has been done with the θ -method, which is a finite difference method. The idea of this θ -method is: compute first $\mathbf{u}^{n+\theta}$ ($0 \leq \theta \leq 1$) at $t^{n+\theta} = t^n + \theta \Delta t$ by

$$\mathbf{M} \frac{\mathbf{u}^{n+\theta} - \mathbf{u}^n}{\theta \Delta t} + \mathbf{N}(\mathbf{u}^{n+\theta}) \mathbf{u}^{n+\theta} + \mathbf{S}(\mathbf{u}^{n+\theta}) \mathbf{u}^{n+\theta} + \frac{1}{\epsilon} \mathbf{L}^T \mathbf{M}_p^{-1} \mathbf{L} \mathbf{u}^{n+\theta} = \mathbf{F}(\mathbf{u}^{n+\theta}) \quad (3.13)$$

$$\text{Then} \quad \mathbf{u}^{n+1} = \frac{1}{\theta} \mathbf{u}^{n+\theta} - \frac{1-\theta}{\theta} \mathbf{u}^n \quad 0 \leq \theta \leq 1 \quad (3.14)$$

The θ -method is conditionally stable for $0 \leq \theta \leq 0.5$. When the penalty function method is used, a time step of $O(\epsilon)$ must be used in order to get a stable scheme for $\theta \leq 0.5$. So the values of θ are restricted to the interval $0.5 \leq \theta \leq 1$. For $\theta = 0.5$ the θ -scheme is a modified Crank-Nicolson scheme, which is a second order method. For $\theta = 1$ the scheme reduces to the first order implicit Euler method [7]. This value is always used in this study.

The cupula

For the motion of the cupula, we must also use a time-integration method. A number of methods are available to do this.

First, we rewrite the equation of motion to get a first order system of differential equations. Using $\xi = y_1$ and $\frac{d\xi}{dt} = y_2$, we get:

$$\begin{bmatrix} y_1 \\ y_2 \end{bmatrix}' = \begin{bmatrix} 0 & 1 \\ -\frac{S}{M} & 0 \end{bmatrix} \begin{bmatrix} y_1 \\ y_2 \end{bmatrix} + \begin{bmatrix} 0 \\ \frac{F}{M} \end{bmatrix} \quad (3.15)$$

or : $y' = \mathbf{A}y + \mathbf{B} = f(t, y)$

A useful time-integration method to solve these equations is a two-step second order Runge Kutta method. If we use this method, the equations become as follows:

$$\begin{cases} y_{n+1}^* = y_n + dt f(t_n, y_n) \\ y_{n+1} = y_n + \frac{dt}{2} [f(t_n, y_n) + f(t_{n+1}, y_{n+1}^*)] \end{cases} \quad (3.16)$$

The first equation, the Euler method, is used as a predictor for the second equation, which is the Trapezium rule. Now we have discretized the equations for the fluid as well as the equations of motion of the cupula. The next step is to couple these equations.

First, an estimate of the velocity of the cupula must be computed to get an estimate of the force acting on the cupula. Then the velocity of the cupula at the new time level can be computed as well as the force acting on the cupula. So, the program must perform four steps in each time step: two SEPRAN computations and two for the Runge Kutta method. That gives the following scheme: Step 1: solving the Navier-Stokes equations using the boundary condition of the computed y_n gives the force \mathbf{B}_n .

Step 2: the Euler method to get an estimate y_{n+1}^* for y_{n+1}

$$y_{n+1}^* = y_n + dt [\mathbf{A}y_n + \mathbf{B}_n] \quad (3.17)$$

Step 3: solving the Navier-Stokes equations using the boundary condition of the estimated y_{n+1}^* gives the estimated force \mathbf{B}_{n+1}^* .

Step 4: the Trapezium rule to get the vector y_{n+1} at the new time level

$$y_{n+1} = y_n + \frac{dt}{2} [\mathbf{A}y_n + \mathbf{B}_n + \mathbf{A}y_{n+1}^* + \mathbf{B}_{n+1}^*] \quad (3.18)$$

3.3.4 Linearization

In all the sets of differential equations till now a nonlinear convective term $\mathbf{N}(\mathbf{u})\mathbf{u}$ appears. This term must be linearized in order to solve the equations. In SEPRAN there are two methods available for linearization:

- Picard linearization
- Newton iteration

For the time-dependent problem one linearization per time step is sufficient. The Picard linearization linearizes the nonlinear convective terms at time level $n + 1$ by substituting the solution of the preceding time level in $N(\mathbf{u}^{n+1})$. The convective terms then become of the form:

$$N(\mathbf{u}^{n+1})\mathbf{u}^{n+1} = N(\mathbf{u}^n)\mathbf{u}^{n+1} \quad (3.19)$$

The Newton iteration linearizes the nonlinear convective terms at time level $n + 1$ as follows:

$$N(\mathbf{u}^{n+1})\mathbf{u}^{n+1} = N(\mathbf{u}^n)\mathbf{u}^{n+1} + N(\mathbf{u}^{n+1})\mathbf{u}^n - N(\mathbf{u}^n)\mathbf{u}^n \quad (3.20)$$

3.3.5 Matrix decomposition

After the time integrations and linearizations, we have a large set of equations. The solution on a new time level is computed numerically using the θ -method:

$$M \frac{\mathbf{u}^{n+\theta} - \mathbf{u}^n}{\theta \Delta t} + [N'(\mathbf{u}^n) + S'(\mathbf{u}^n) + \frac{1}{\epsilon} \mathbf{L}^T M_p^{-1} \mathbf{L}] \mathbf{u}^{n+\theta} = \mathbf{F}(\mathbf{u}^{n+\theta}) \quad (3.21)$$

$$\text{Then } \mathbf{u}^{n+1} = \frac{1}{\theta} \mathbf{u}^{n+\theta} - \frac{1-\theta}{\theta} \mathbf{u}^n \quad 0 \leq \theta \leq 1 \quad (3.22)$$

with $N'(\mathbf{u}^n)$ and $S'(\mathbf{u}^n)$ the results of the Picard or Newton linearization. Now define \mathbf{A} and \mathbf{b} as:

$$\mathbf{A} = M + \theta \Delta t [N'(\mathbf{u}^n) + S'(\mathbf{u}^n) + \frac{1}{\epsilon} \mathbf{L}^T M_p^{-1} \mathbf{L}] \quad (3.23)$$

$$\mathbf{b} = M + \theta \Delta t \mathbf{F}(\mathbf{u}^{n+\theta}) \quad (3.24)$$

Now the set of equations is reduced to $\mathbf{A}x = \mathbf{b}$ in which $x = \mathbf{u}^{n+\theta}$ is the unknown solution vector. This linear set can be solved by using Gaussian Elimination. [1]

Faint, illegible text, possibly bleed-through from the reverse side of the page. The text is too light to transcribe accurately.

Chapter 4

Results

4.1 The 2D channel geometry

In the research of Meeuwissen [6], most of the time an axisymmetric geometry was used and the radius of the cupula was always taken 0.3 mm. The upper wall was chosen at a relative large distance from the top of the cupula. From the measurements of Tsang, it appeared that the radius of one of the cupulae is about 0.6 mm. He also discovered that the upper wall is at a distance of 0.9 mm from the bottom wall. Therefore, van Hengel (unpublished data) tried to compute the flow with the 2D model and took $r = 0.6$ mm. He found an unstable solution. The maximum radius at which the cupula moved in a stable fashion was 0.55 mm. So, the following questions arose: is there a maximum size of the cupula, beyond which it is not possible to compute the flow and if so, is this a numerical or a physical limit?

The direction in which the cupula starts to move in the first time step, determines whether or not the solution is stable. This in turn depends on the sign of the force on the cupula after the first time step¹. If the sign is positive, the cupula starts to move in the right direction, which is of course the same as the direction of the inflow. If the sign is negative, the cupula starts to move in the wrong direction and eventually the solution will explode. So, we must assure that the force on the cupula after the first time step is positive. The adaptation in the boundary condition given by equations 2.6 and 2.7 was used.

Now we can look at the minimum number of time steps per period required to get a positive force after the first time step. The results for a frequency of 100 Hz and inflow velocity $8.9075 \cdot 10^{-9}$ m/s are shown in table 4.1.

It is clear that the number of required time steps increases very fast if the radius becomes larger than 0.55 mm. With the fastest available computer, CIWI11, one time step takes about 19 seconds, so hundred time steps will take 32 minutes. For a periodic solution, at least five periods must be computed, so the computation time becomes at least 13 hours if $r = 0.6$ mm and $\delta = 0.25r$.

¹Note that there are two SEPRAN runs in one time step

Table 4.1: Number of time steps per period for different radii

δ	$r=0.50$	$r=0.55$	$r=0.56$	$r=0.57$	$r=0.58$	$r=0.59$	$r=0.60$
$0.05r$	31	151	285	752	4148	21247	45286
$0.10r$	25	97	159	316	917	5881	24973
$0.15r$	21	67	101	171	356	1161	8280
$0.20r$	17	50	70	106	185	410	1543
$0.25r$	15	38	51	72	113	204	485

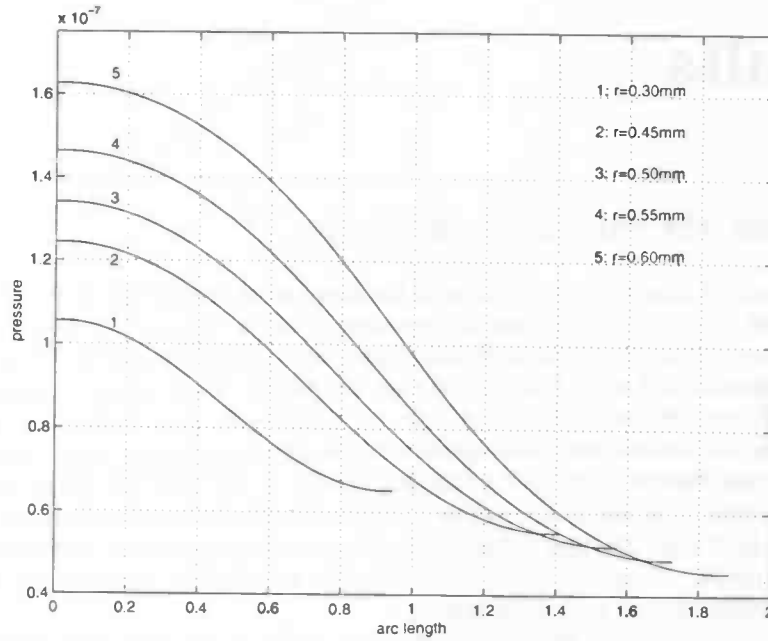


Figure 4.1: Pressure profile on the cupula for different values of r

Now, let's look what is happening with the force on the cupula in the first time step. The force computed after the first SEPRAN run, giving the first boundary condition with u_{cupula} greater than zero, plays an important role. This value contains the pressure force and the viscous force. It turns out that the value, computed after the first SEPRAN run, is for more than 90 % determined by the pressure profile on the cupula. The results for $r = 0.3, 0.45, 0.5, 0.55$ and 0.6 mm are shown in figure 4.1. The values of the force on the cupula, the pressure force, the viscous force, the maximum levels of the pressure, p_{max} and the resulting u_{cupula} are given in table 4.2.

The value of u_{cupula} is at all radii larger than the inflow velocity, $8.9075 \cdot 10^{-9}$ m/s. This means that the flux across the vertical contour above the cupula must compensate the relatively large flux across the cupula contour.

Table 4.2:

r	F	F_{pres}	F_{visc}	p_{max}	u_{cupula}
0.30	$1.0289 \cdot 10^{-8}$	$9.6725 \cdot 10^{-9}$	$6.1690 \cdot 10^{-10}$	$1.0555 \cdot 10^{-7}$	$1.1260 \cdot 10^{-8}$
0.45	$2.6052 \cdot 10^{-8}$	$2.4979 \cdot 10^{-8}$	$1.0735 \cdot 10^{-9}$	$1.2442 \cdot 10^{-7}$	$1.2671 \cdot 10^{-8}$
0.50	$3.4312 \cdot 10^{-8}$	$3.3032 \cdot 10^{-8}$	$1.2801 \cdot 10^{-9}$	$1.3403 \cdot 10^{-7}$	$1.3517 \cdot 10^{-8}$
0.55	$4.4991 \cdot 10^{-8}$	$4.3458 \cdot 10^{-8}$	$1.5337 \cdot 10^{-9}$	$1.4636 \cdot 10^{-7}$	$1.4648 \cdot 10^{-8}$
0.60	$5.9168 \cdot 10^{-8}$	$5.7311 \cdot 10^{-8}$	$1.8568 \cdot 10^{-9}$	$1.6263 \cdot 10^{-7}$	$1.6187 \cdot 10^{-8}$

Table 4.3: Number of time steps per period for different radii

δ	$r=0.50$	$r=0.55$	$r=0.56$	$r=0.57$	$r=0.58$	$r=0.59$	$r=0.60$
$0.05r$	28	126	224	520	2180	14549	37416
$0.10r$	21	73	112	195	434	1642	11775
$0.15r$	17	48	66	100	172	369	1280
$0.20r$	14	33	44	61	91	152	319
$0.25r$	11	25	31	40	56	83	138

This compensated flux is $0.9 u_{inflow} - u_{cupula}r$. So, knowing that u_{cupula} increases if r increases, the compensated flux must decrease strongly. Therefore, backward flow above the cupula may occur if r is increased and this may lead to a negative F after the first time step. So, it is not hard to understand that the number of required time steps will increase strongly at a certain radius.

A way to decrease the number of required time steps, is to change the adaptation in the boundary condition of the cupula, such that the flux across the cupula contour decreases. This means that on the average u_{cupula} decreases, so the force on the cupula decreases. From this moment, we take the following boundary condition at the cupula:

$$\frac{d\xi}{dt} = u_{cupula} \quad \text{for } \delta \leq y \leq r \quad (4.1)$$

$$\frac{d\xi}{dt} = \left(\frac{1}{2} - \frac{1}{2} \cos\left(\frac{\pi y}{\delta}\right) \right) u_{cupula} \quad \text{for } 0 \leq y \leq \delta \quad (4.2)$$

The minimum number of time steps per period is given in table 4.3

So, it is clear that the number of time steps decreases strongly if we change the adaptation in the boundary condition of the cupula. Now, let's look what happens in the amplitude and phase pictures if we enlarge the cupula. The results are shown in figure 4.2. The resonance frequency decreases if r is increased, in spite of the fact that S is chosen as $\omega_{res}^2 M$

Another problem that occurs, is the fact that the approximation converges very slowly to a certain solution at some frequencies with a decrease of the time step. To compare different radii at frequencies near the resonance frequency, we have to take different frequencies. The estimate of the resonance frequency is 115, 110 and 105 Hz for $r = 0.3, 0.45$ and 0.5 mm.

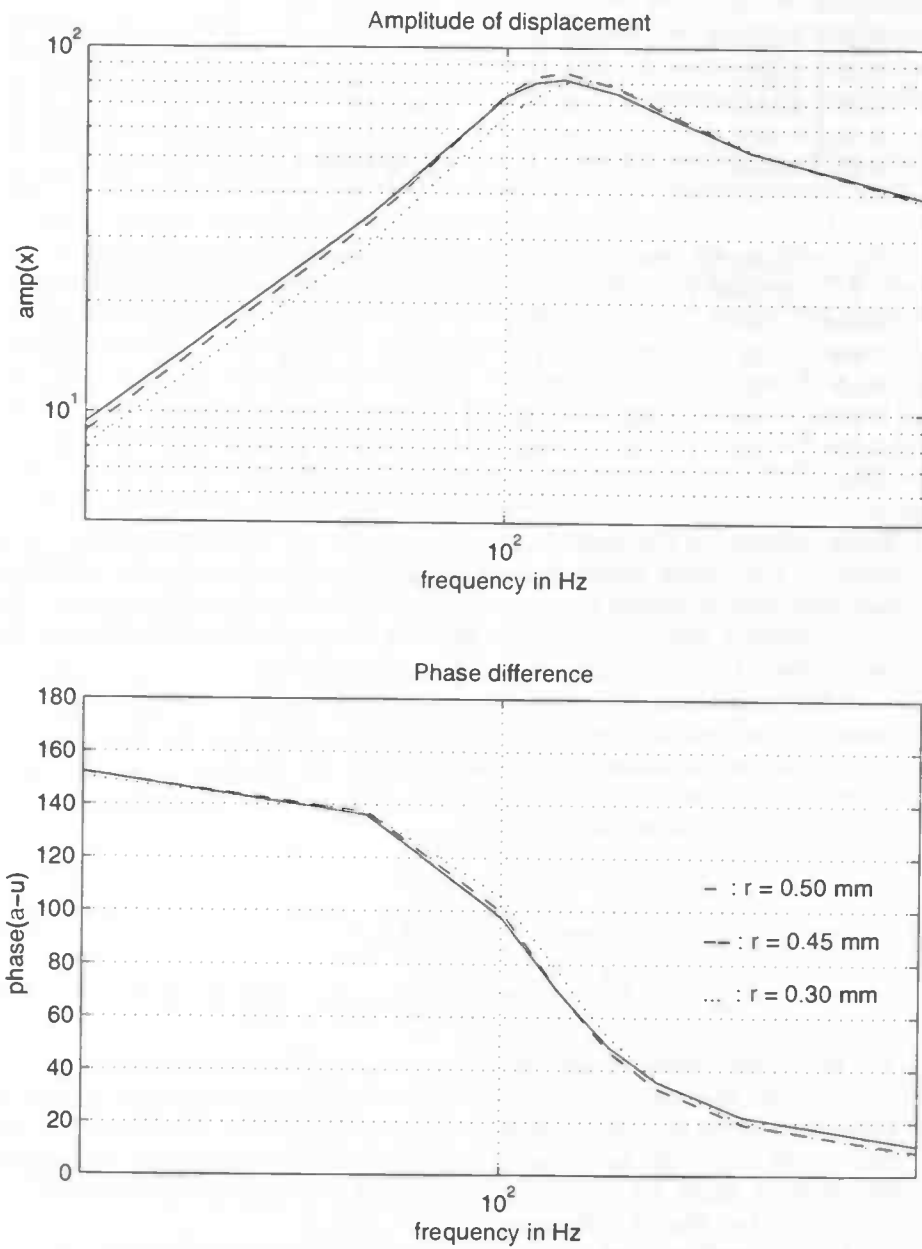


Figure 4.2: Amplitude of displacement and phase difference as function of the frequency (50 till 200 Hz).

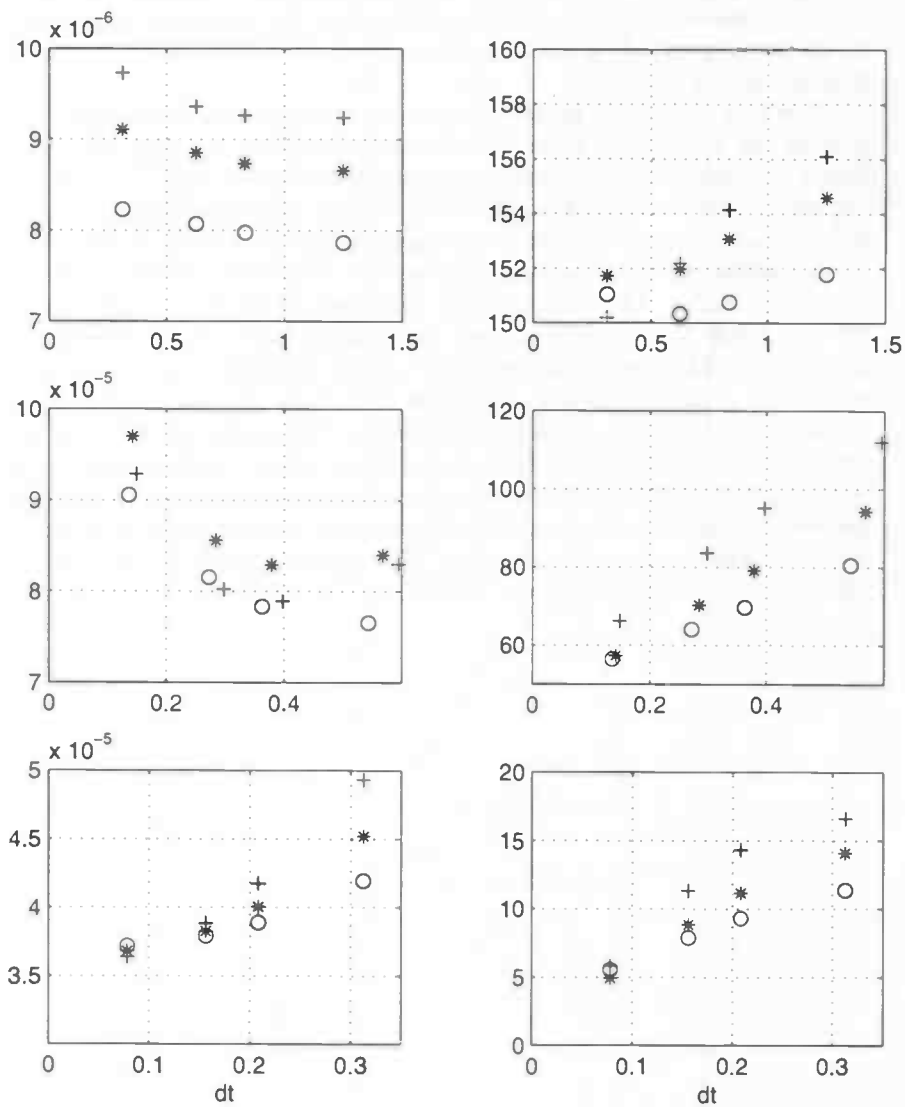


Figure 4.3: Solution as function of stepsize dt . \circ : $r=0.30$ mm, $*$: $r=0.45$ mm, $+$: $r=0.50$ mm. On the left side, the amplitudes of displacement are shown and on the right side the phase differences are shown. The frequency in the first row is 50 Hz, in the second row f_{res} and in the third row 200 Hz.

The results are shown in figure 4.3. From figure 4.3 we may conclude that at 50 Hz the phase difference converges for the radii we used, but the amplitude diverges if r is increased. At 200 Hz the amplitude converges, but the phase difference seems to diverge. At frequencies near f_{res} , the phase difference seems to converge, although it decreases strongly if dt is increased. The amplitude diverges in this case.

Now let's look at the horizontal velocity at some cross-sections and the pressure on the upper wall, bottom wall and cupula. The velocity pictures are labelled in reading order at the cross sections a) $x = -r-1$, b) $x = -r-0.1$, c) $x = -r$, d) $x = -0.5r$, e) $x = 0$ and f) on the outflow boundary. These cross-sections are shown in figure 4.4 and they are taken at the time of zero inflow. The plots g) to l) show the same cross-sections as the plots a) to f), but at the time of maximum inflow. The velocity plots are shown in the figures 4.5, 4.6 and 4.7. On the x -axis the distance between the bottom wall and the specific point is plotted. In the pressure pictures 4.8, 4.9 and 4.10, the pressure is plotted as a function of the distance to the inflow boundary. On the outflow boundary, the horizontal velocity develops into the Searl-Womersley profile. The most remarkable fact is that at the time of maximum inflow, backward flow occurs on the cross-section above the cupula when the frequency is about f_{res} and r is increased. Further, the pressure profile shows a reverse gradient in the area of the cupula at the time of zero inflow. When the frequency is 50 or 200 Hz, no remarkable effects appear in the pictures.

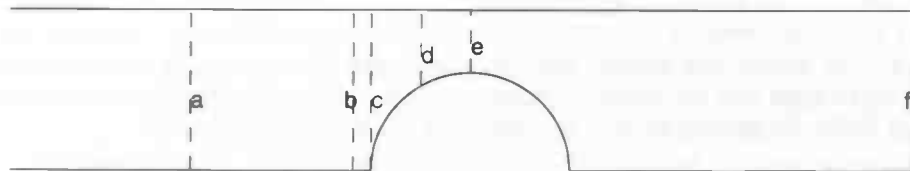


Figure 4.4: The different cross-sections

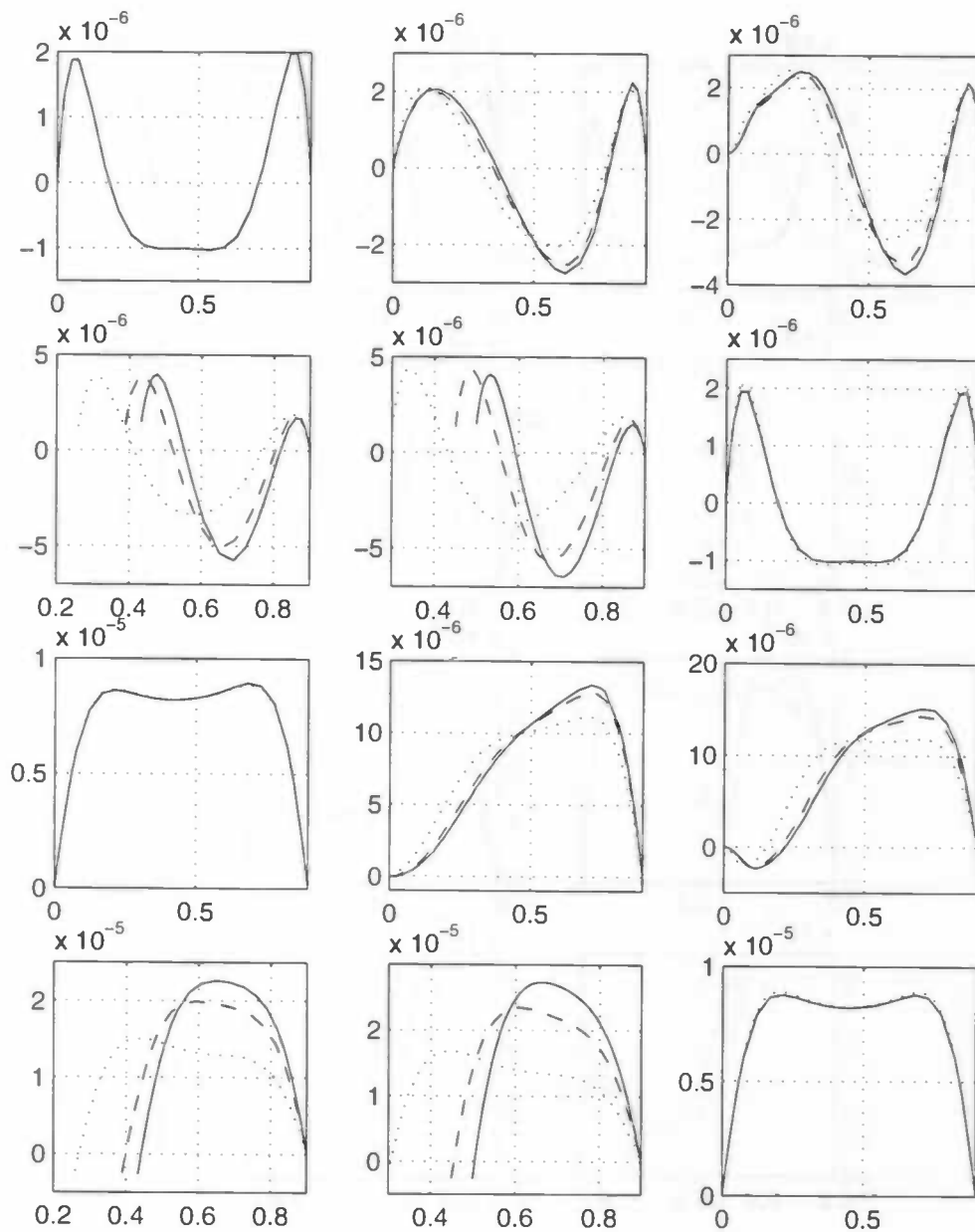


Figure 4.5: The horizontal velocity at the time of zero (pictures a to f) and maximum inflow (pictures g to i) at different cross-sections (see figure 4.4) for $f = 50$ Hz, $r=0.3$ mm (dotted line), $r = 0.45$ mm (dashed line) and $r = 0.5$ mm (solid line), $n = 64$. In the pictures f and i the solid lines are the approximations and the dotted lines are the Womersley profiles.

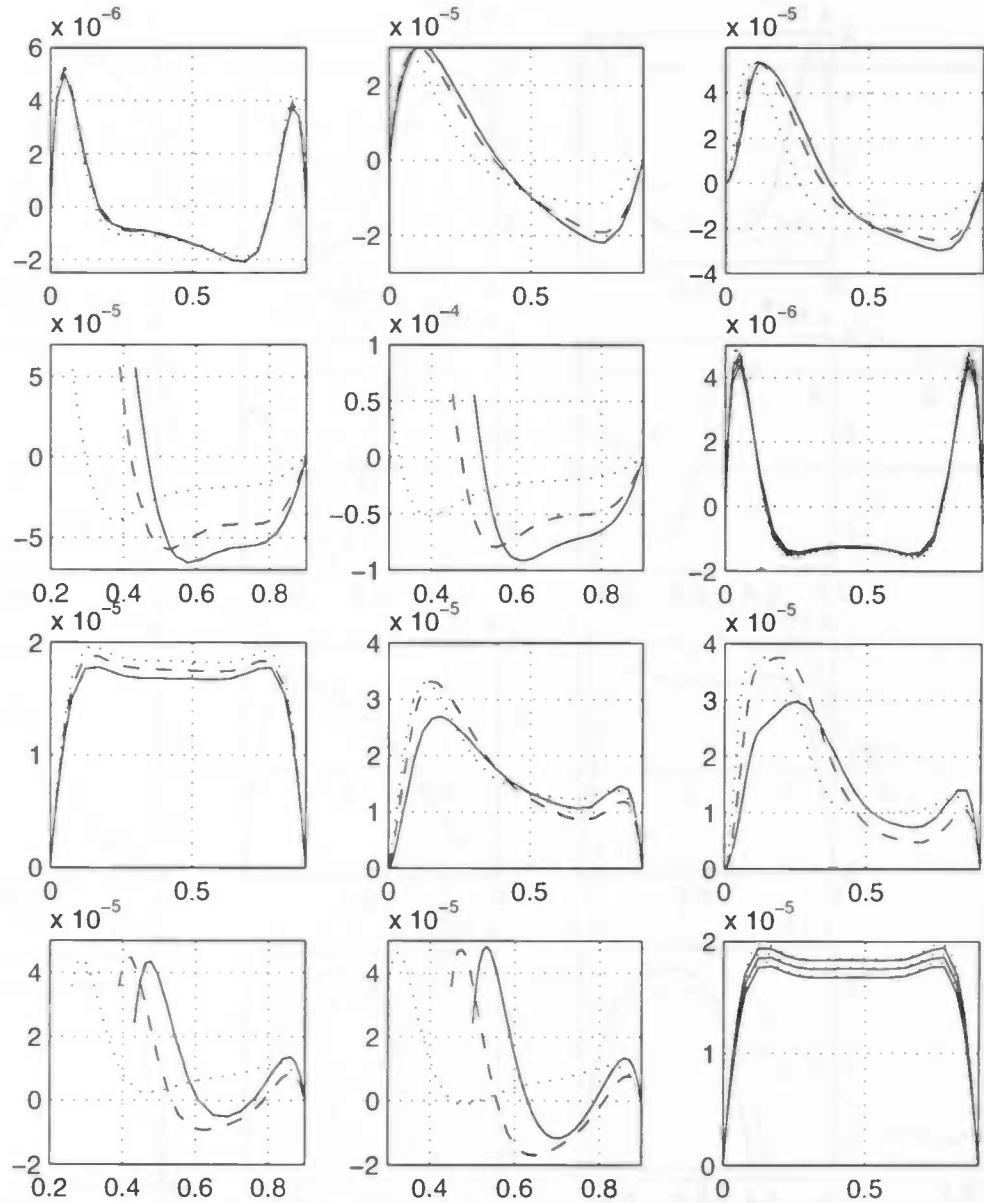


Figure 4.6: The horizontal velocity at the time of zero (pictures a to f) and maximum inflow (pictures g to i) at different cross-sections (see figure 4.4) for $f = f_{res}$, $r=0.3$ mm (dotted line), $r = 0.45$ mm (dashed line) and $r = 0.5$ mm (solid line), $n = 64$. In the pictures f and i the solid lines are the approximations and the dotted lines are the Womersley profiles.

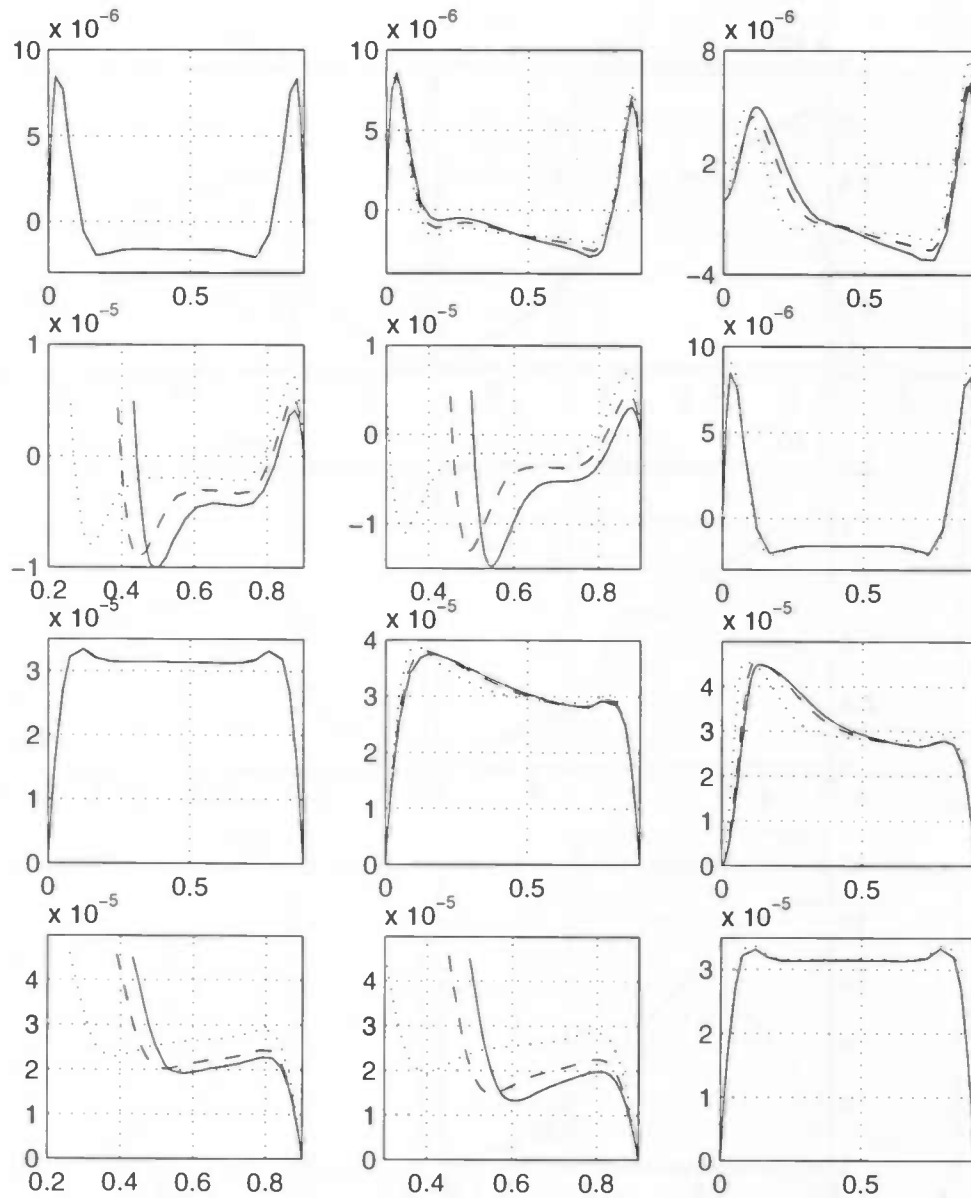


Figure 4.7: The horizontal velocity at the time of zero (pictures a to f) and maximum inflow (pictures g to l) at different cross-sections (see figure 4.4) for $f = 200$ Hz, $r=0.3$ mm (dotted line), $r = 0.45$ mm (dashed line) and $r = 0.5$ mm (solid line), $n = 64$. In the pictures f and l the solid lines are the approximations and the dotted lines are the Womersley profiles.

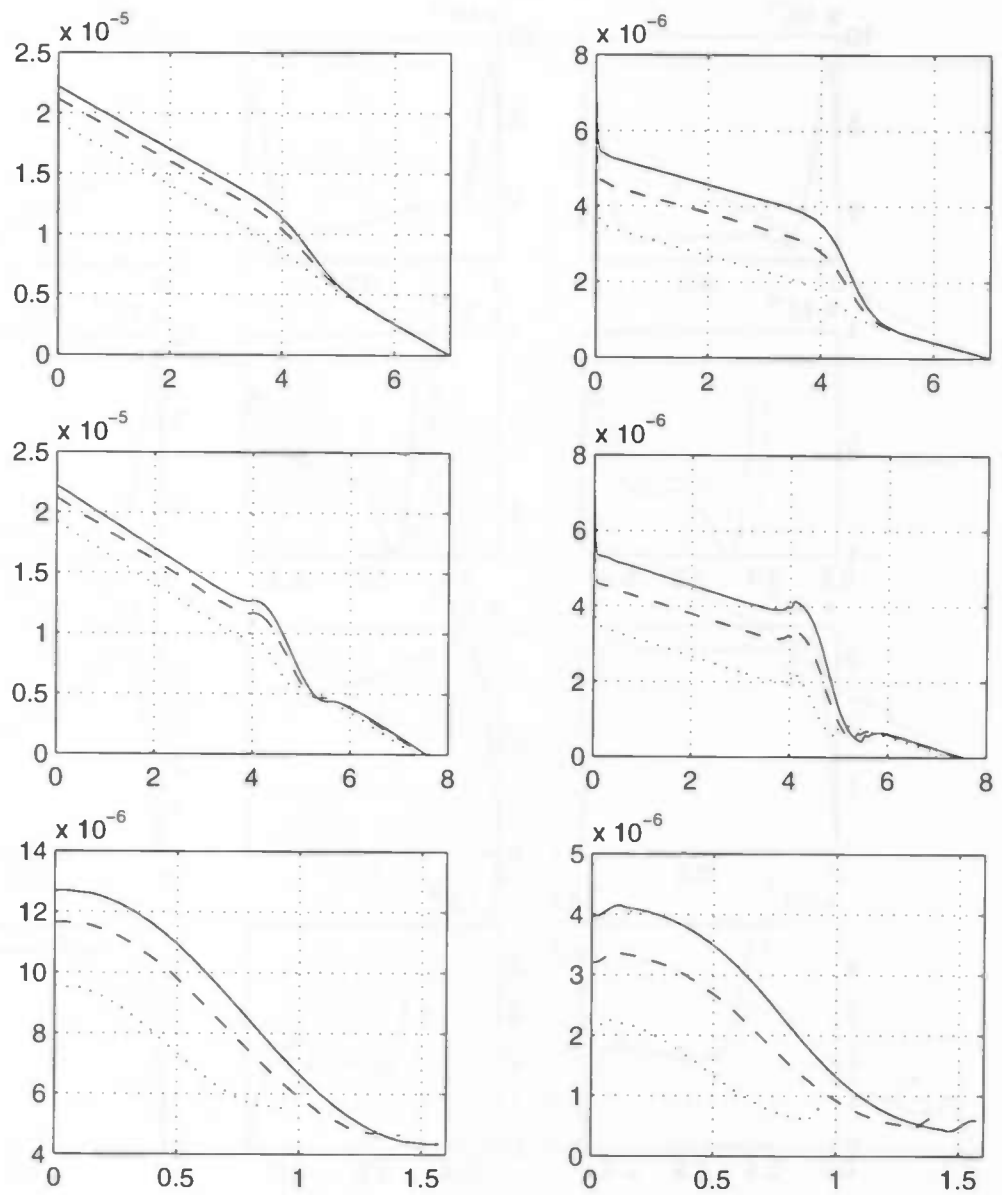


Figure 4.8: The pressure profile at the upper wall (first row), bottom wall (second row) and cupula (third row) for the times of zero inflow (left side) and maximum inflow (right side) for $f = 50$ Hz, $r = 0.3$ mm (dotted line), $r = 0.45$ mm (dashed line) and $r = 0.5$ mm (solid line), $n = 64$.

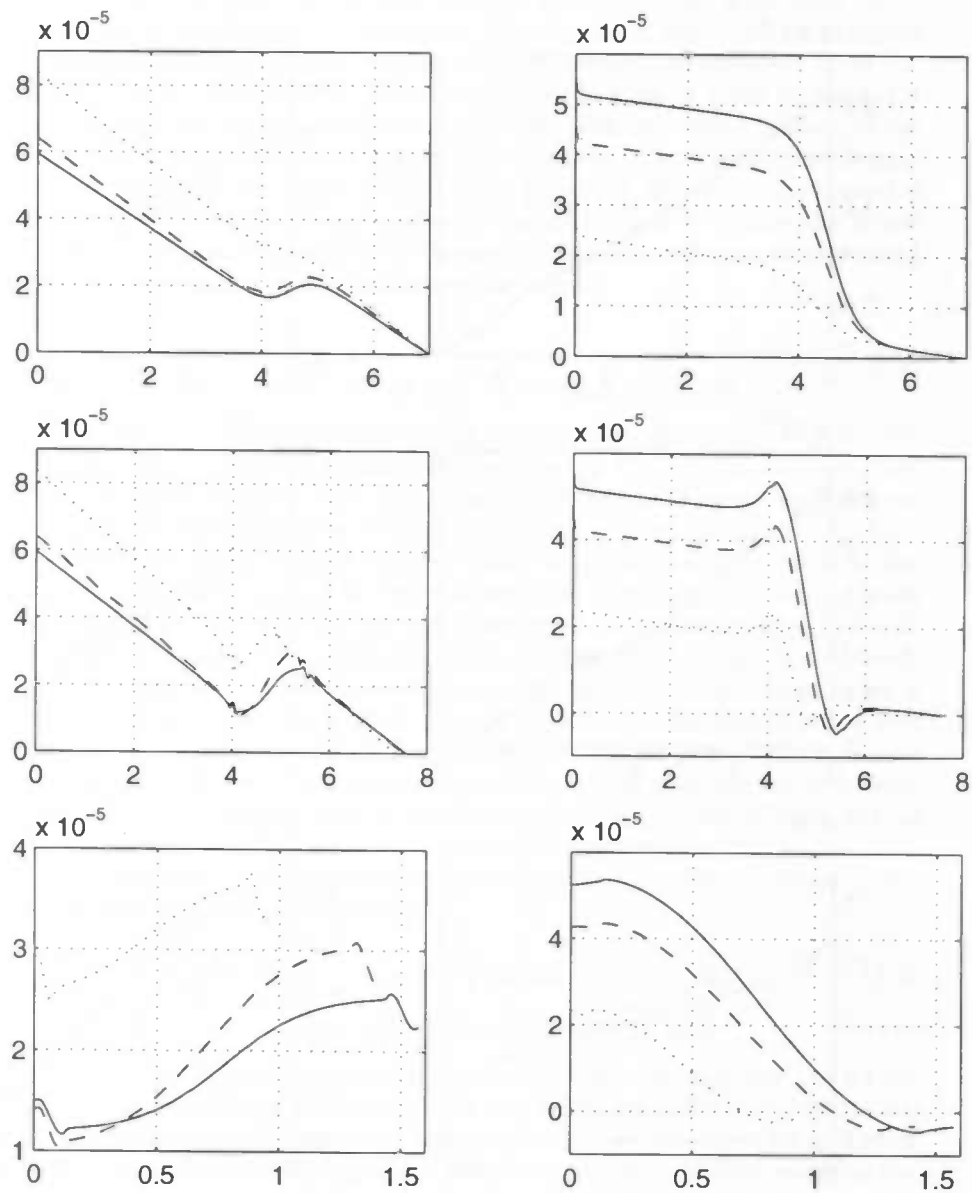


Figure 4.9: The pressure profile at the upper wall (first row), bottom wall (second row) and cupula (third row) for the times of zero inflow (left side) and maximum inflow (right side) for $f = f_{res}$, $r = 0.3$ mm (dotted line), $r = 0.45$ mm (dashed line) and $r = 0.5$ mm (solid line), $n = 64$.

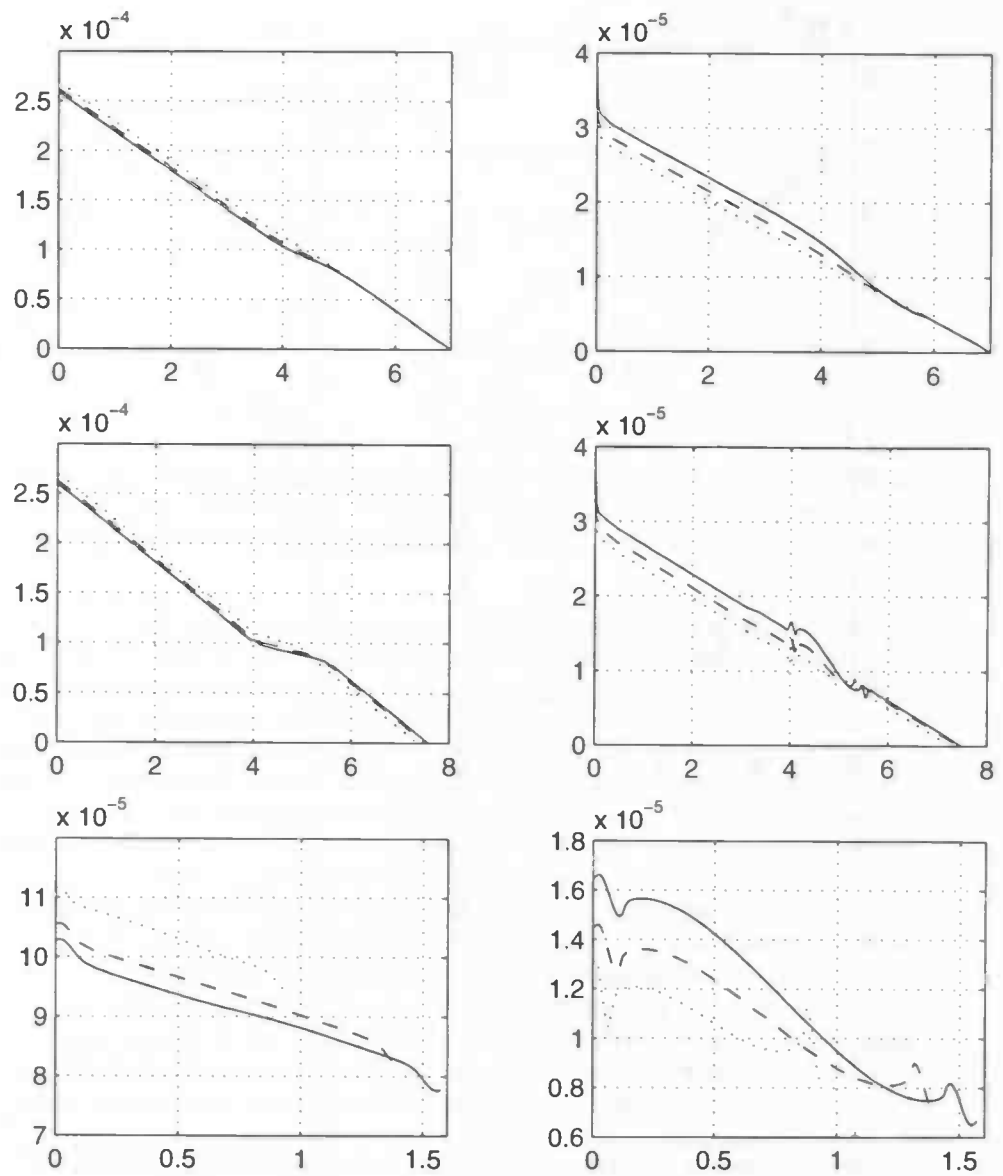


Figure 4.10: The pressure profile at the upper wall (first row), bottom wall (second row) and cupula (third row) for the times of zero inflow (left side) and maximum inflow (right side) for $f = 200$ Hz, $r = 0.3$ mm (dotted line), $r = 0.45$ mm (dashed line) and $r = 0.5$ mm (solid line), $n = 64$.

So, knowing that the approximation does not always converge to a certain solution, especially near f_{res} and knowing that the required number of time steps increases very rapidly if the cupula is enlarged above 0.55 mm, something has to be changed to overcome these problems. The way to do this, without changing the physics of the model, is to change the time-integration method. From the research done by Dijkstra [4], it appeared that the implicit Euler method is a useful method for the time-integration of a fluid with oscillating inflow. So the choice falls to the equations of motion of the cupula. The second order Runge Kutta method that was used to solve these equations, is a predictor-corrector method [3]. The simplest way to change this method is to change the factor with which the predictor is taken in the corrector. This coefficient will be called c_{pred} , so the equations of motion become as follows:

$$\begin{cases} \mathbf{y}_{n+1}^* = \mathbf{y}_n + dt f(t_n, \mathbf{y}_n) \\ \mathbf{y}_{n+1} = \mathbf{y}_n + dt [(1 - c_{pred}) f(t_n, \mathbf{y}_n) + c_{pred} f(t_{n+1}, \mathbf{y}_{n+1}^*)] \end{cases} \quad (4.3)$$

First, the adaptation in the boundary condition is taken at the cupula with $\delta = 0.25r$. The results with different choices of c_{pred} , $r = 0.3$ mm and frequency 115 Hz are shown in figure 4.11. The figure shows the amplitude of displacement ($\text{amp}(\xi)$), the amplitude of the velocity ($\text{amp}(u_{cupula})$) and the amplitude of the force ($\text{amp}(F)$) on the cupula together with the phase difference between the inflow velocity and u_{cupula} . The figure shows that choosing c_{pred} below 0.5 leads to a different behaviour in the way the approximation converges. If $c_{pred} \approx 0.3$, the solution changes only a little bit if the number of time steps is increased. Decreasing the factor leads to a slower convergence. So there seems to be a kind of optimum factor, with which the real solution can be approximated well taking only a low number of time steps. Also it follows that if the optimum choice is at a value below 0.5, the velocity of the cupula after the first time step is lowered. So a problem with $r = 0.6$ mm might be computed using not so much computing time.

From this moment the adaptation in the boundary condition is taken at the bottom wall, with $\delta = 0.1 r$ giving:

$$u = \left(\frac{1}{2} + \frac{1}{2} \cos \left(\frac{\pi(|x| - r)}{\delta} \right) \right) u_{cupula} \quad \text{for } r \leq |x| \leq r + \delta \quad (4.4)$$

$$u = 0 \quad \text{for the other parts of the bottom wall} \quad (4.5)$$

The results for different choices of c_{pred} , $r = 0.3$ mm and frequency 110 Hz are shown in figure 4.12 and the results with $r = 0.6$ mm and frequency 90 Hz are shown in figure 4.13. When $r = 0.3$ mm, the best choice is $c_{pred} \approx 0.3$ and when $r = 0.6$ mm it is ≈ 0.2 . Taking these optimum coefficients, we can compute the velocity of the cupula after the first time step for different radii. It turns out that u_{cupula} stays approximately the same for each frequency. Now the question arises if the optimum choice is the same for all frequencies. Therefore the results for $r = 0.3$ mm, $f = 50$ and $f = 200$ Hz are shown in figures 4.14 and 4.15.

The solution at 50 Hz changes only a few percents when dt is decreased, so the choice of c_{pred} makes very little difference. At 200 Hz, the amplitude of displacement changes only a few percents, but the amplitude of the force changes

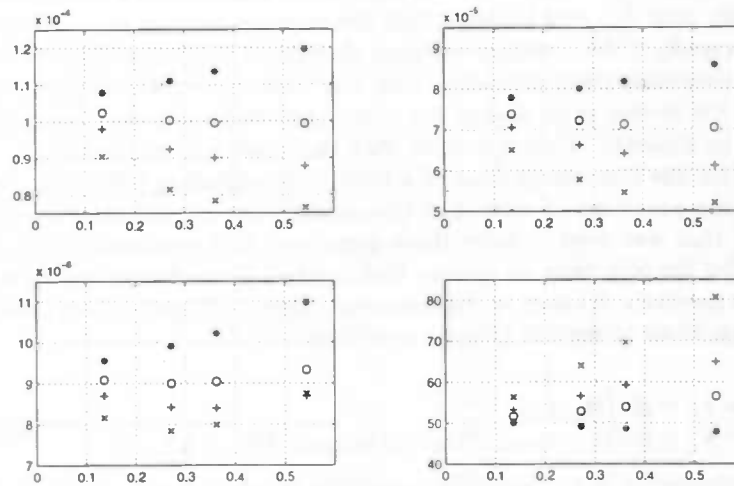


Figure 4.11: $\text{Amp}(\xi)$, $\text{amp}(u_{cupula})$, $\text{amp}(F)$ and phase difference for different choices of c_{pred} : *: $c=0.25$, 0: $c=0.33$, +: $c=0.4$, x: $c=0.5$. The window is taken at the cupula (see equations 4.1 and 4.2), $r=0.3$ mm, $f=115$ Hz.

more than 10 % if c_{pred} is chosen far from the optimum choice at f_{res} . So the optimum choice can be taken the same for all frequencies. Now, the amplitude and phase pictures with changed c_{pred} are shown in figure 4.16. When the cupula is enlarged to 0.6 mm, the resonance frequency decreases to about 90 Hz. At high frequencies, the phase difference becomes slightly negative and at low frequencies it decreases when f is decreased. The peak in the amplitude does not change much (90-100 nm) when the cupula is enlarged. The velocity pictures with changed c_{pred} are shown in the figures 4.17, 4.18 and 4.19. The pressure pictures are shown in the figures 4.20, 4.21 and 4.22. The used estimate of f_{res} are 110, 95 and 90 Hz for $r = 0.3, 0.55$ and 0.6 mm. At the resonance frequency strong backward flow appears above the cupula at the time of maximum inflow and at the time of zero inflow a strong reverse pressure gradient appears. This gradient increases when the cupula is enlarged. In figure 4.21 the pressure level becomes negative at the time of zero inflow. This can be explained by noting that SEPRAN always sets the pressure level on the outflow boundary to zero. At other frequencies no remarkable effects can be seen.

Concluding, we may say that from the results obtained, there does not seem to be a numerical limit around $r = 0.6$ mm. With a suitable choice of c_{pred} , it is possible to compute an approximation which does not change much when the time step is decreased. Looking at the velocity and pressure pictures, there is no reason to assume that strange physical effects appear when the cupula is enlarged to 0.6 mm.

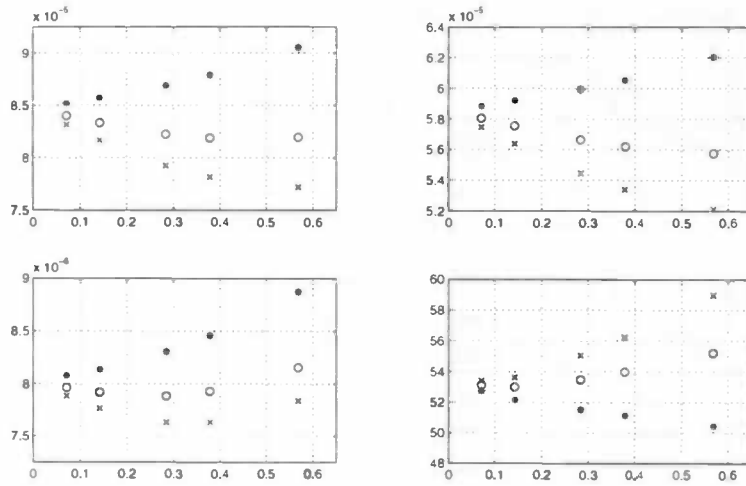


Figure 4.12: $\text{Amp}(\xi)$, $\text{amp}(u_{cupula})$, $\text{amp}(F)$ and phase difference for different choices of c_{pred} . *: $c=0.25$, 0: $c=0.3$, x: $c=0.33$. The window in the boundary conditions is taken at the bottom wall, (see equations 4.4 and 4.5), $r=0.3$ mm, $f=110$ Hz.

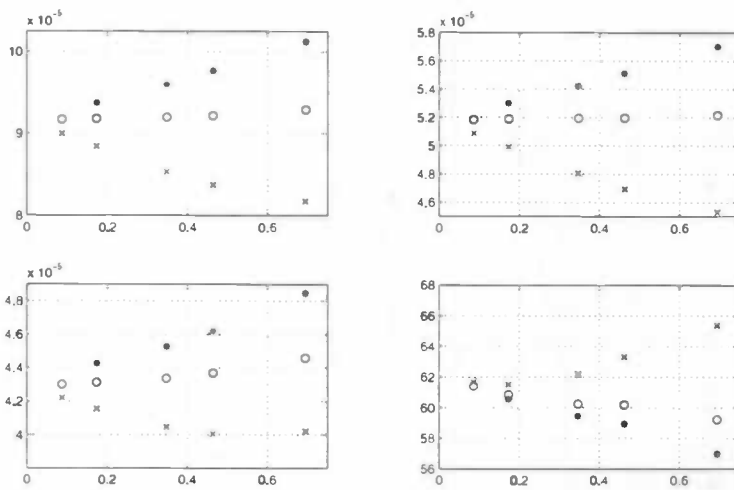


Figure 4.13: $\text{Amp}(\xi)$, $\text{amp}(u_{cupula})$, $\text{amp}(F)$ and phase difference for different choices of c_{pred} . *: $c=0.167$, 0: $c=0.2$, x: $c=0.25$. The window in the boundary conditions is taken at the bottom wall (see equations 4.4 and 4.5), $r=0.6$ mm, $f=90$ Hz.

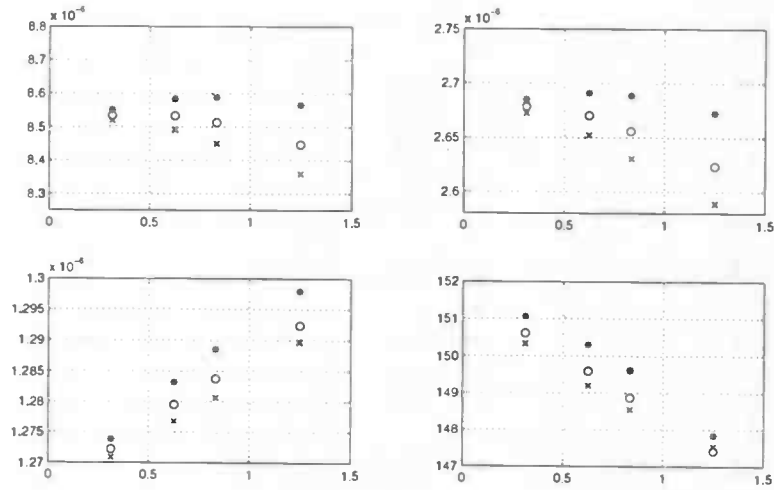


Figure 4.14: $\text{Amp}(\xi)$, $\text{amp}(u_{cupula})$, $\text{amp}(F)$ and phase difference for different choices of c_{pred} . *: $c=0.167$, 0: $c=0.2$, x: $c=0.25$. The window in the boundary conditions is taken at the bottom wall (see equations 4.4 and 4.5), $r=0.3$ mm, $f=50$ Hz.

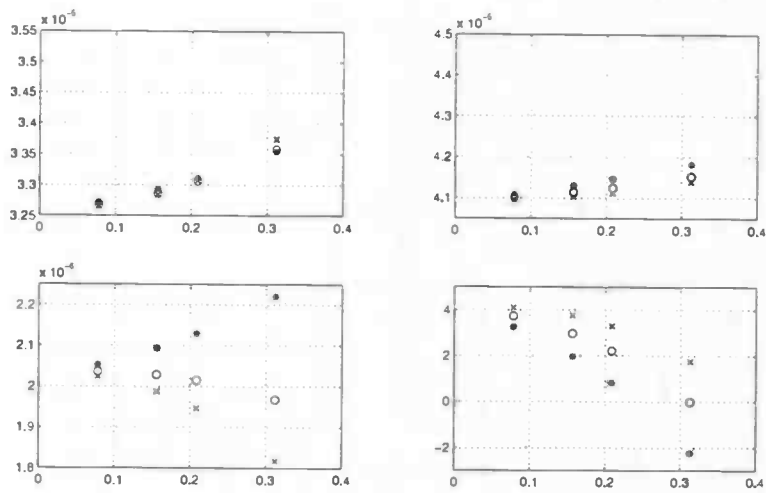


Figure 4.15: $\text{Amp}(\xi)$, $\text{amp}(u_{cupula})$, $\text{amp}(F)$ and phase difference for different choices of c_{pred} . *: $c=0.167$, 0: $c=0.2$, x: $c=0.25$. The window in the boundary conditions is taken at the bottom wall (see equations 4.4 and 4.5), $r=0.3$ mm, $f=200$ Hz.

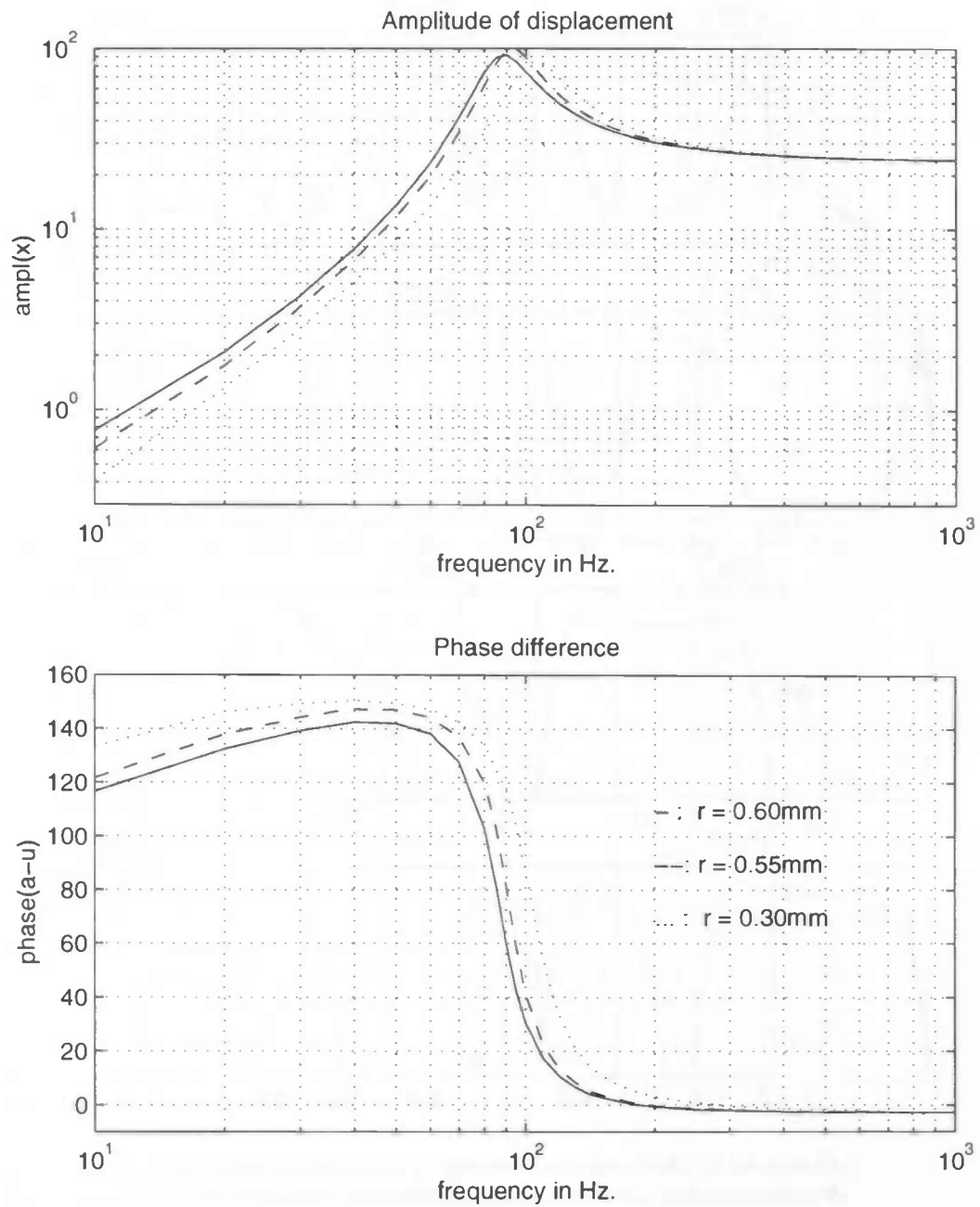


Figure 4.16: Amplitude of displacement and phase difference between inflow velocity and velocity of the cupula as function of the frequency.

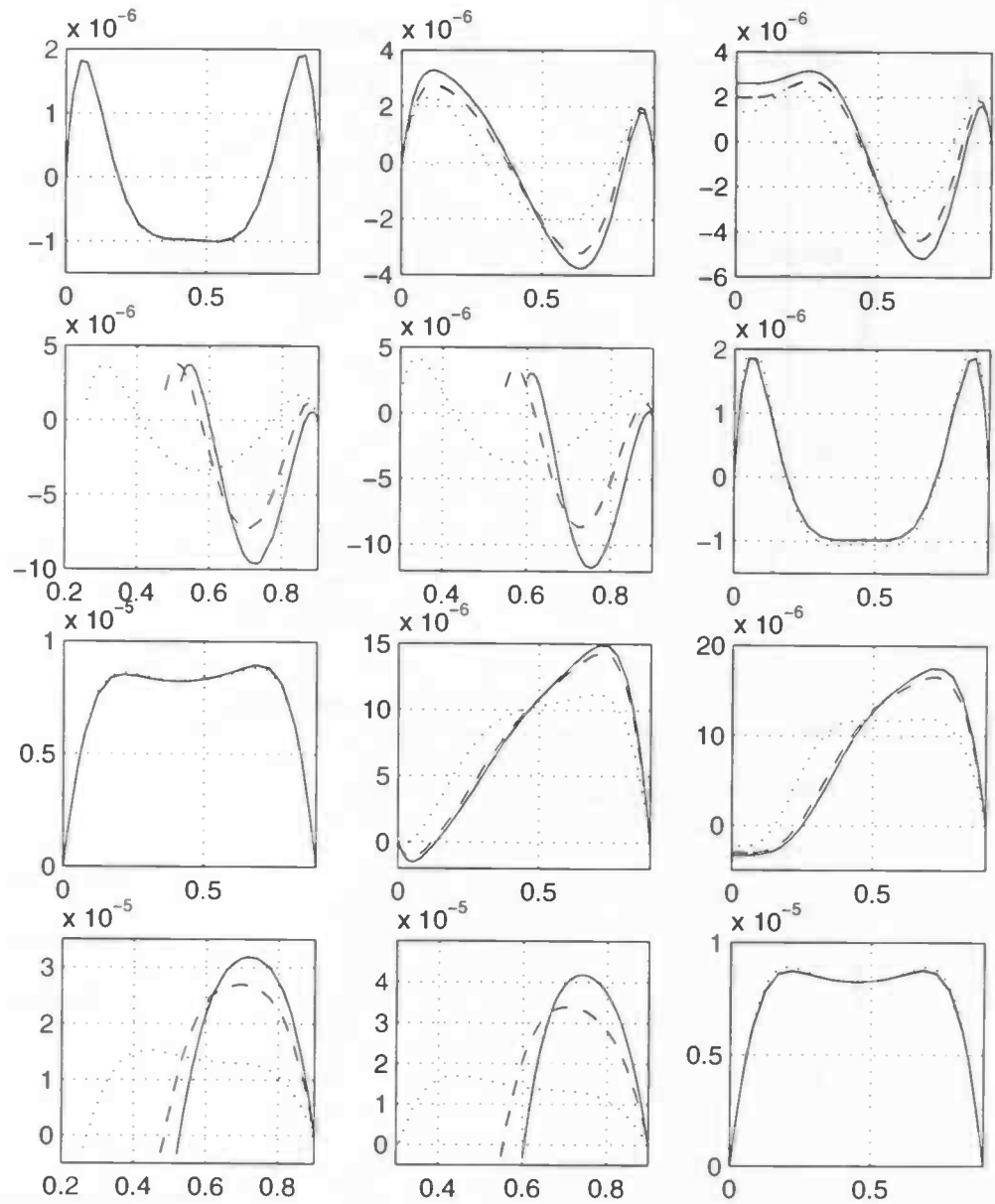


Figure 4.17: The horizontal velocity at the time of zero (pictures a to f) and maximum inflow (pictures g to i) at different cross-sections (see figure 4.4) for $f = 50$ Hz, $r=0.3$ mm (dotted line), $r = 0.55$ mm (dashed line) and $r = 0.6$ mm (solid line), $n = 32$. In the pictures f and i the solid lines are the approximations and the dotted lines are the Womersley profiles.

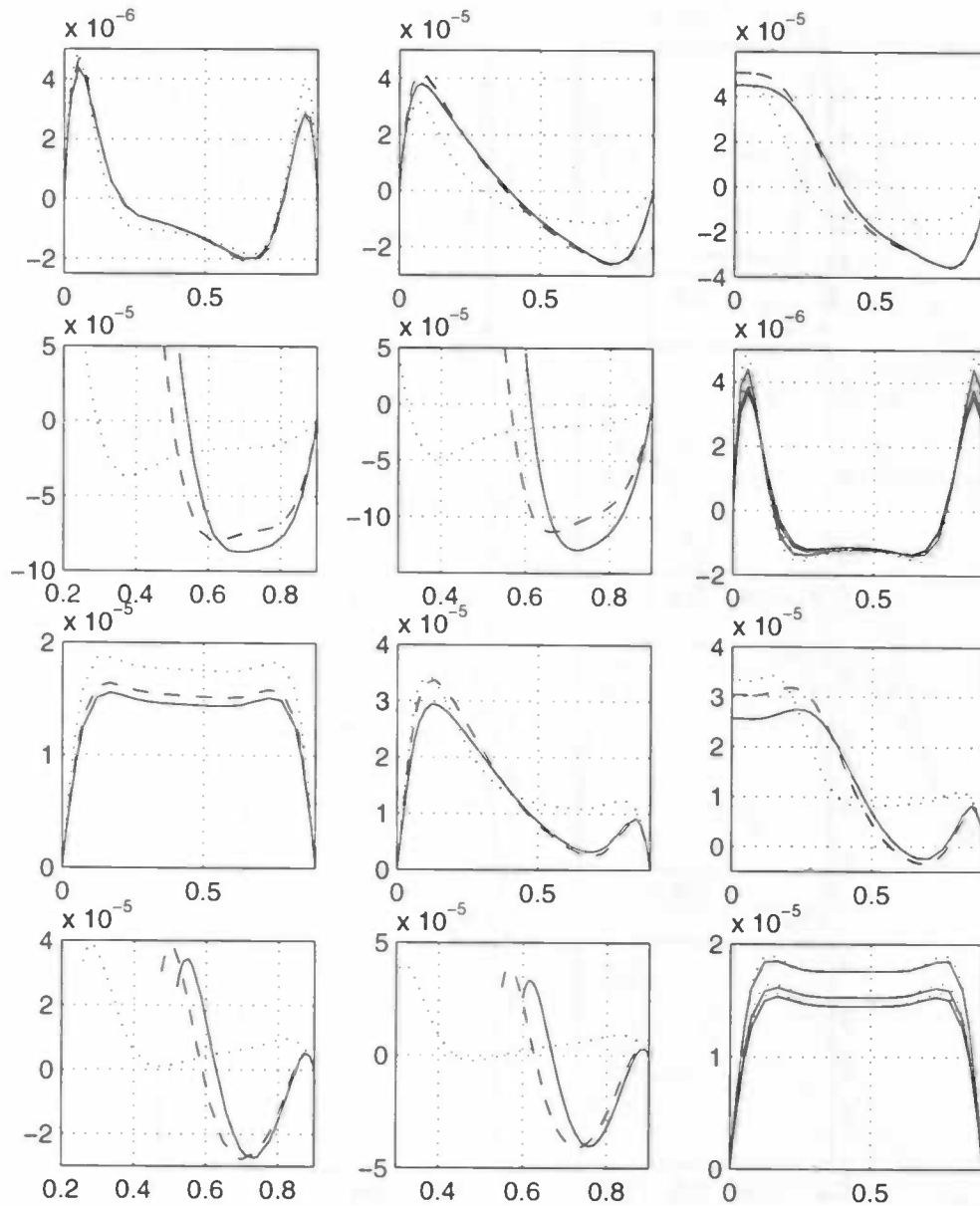


Figure 4.18: The horizontal velocity at the time of zero (pictures a to f) and maximum inflow (pictures g to l) at different cross-sections (see figure 4.4) for $f = f_{res}$, $r=0.3$ mm (dotted line), $r = 0.55$ mm (dashed line) and $r = 0.6$ mm (solid line), $n = 32$. In the pictures f and l the solid lines are the approximations and the dotted lines are the Womersley profiles.

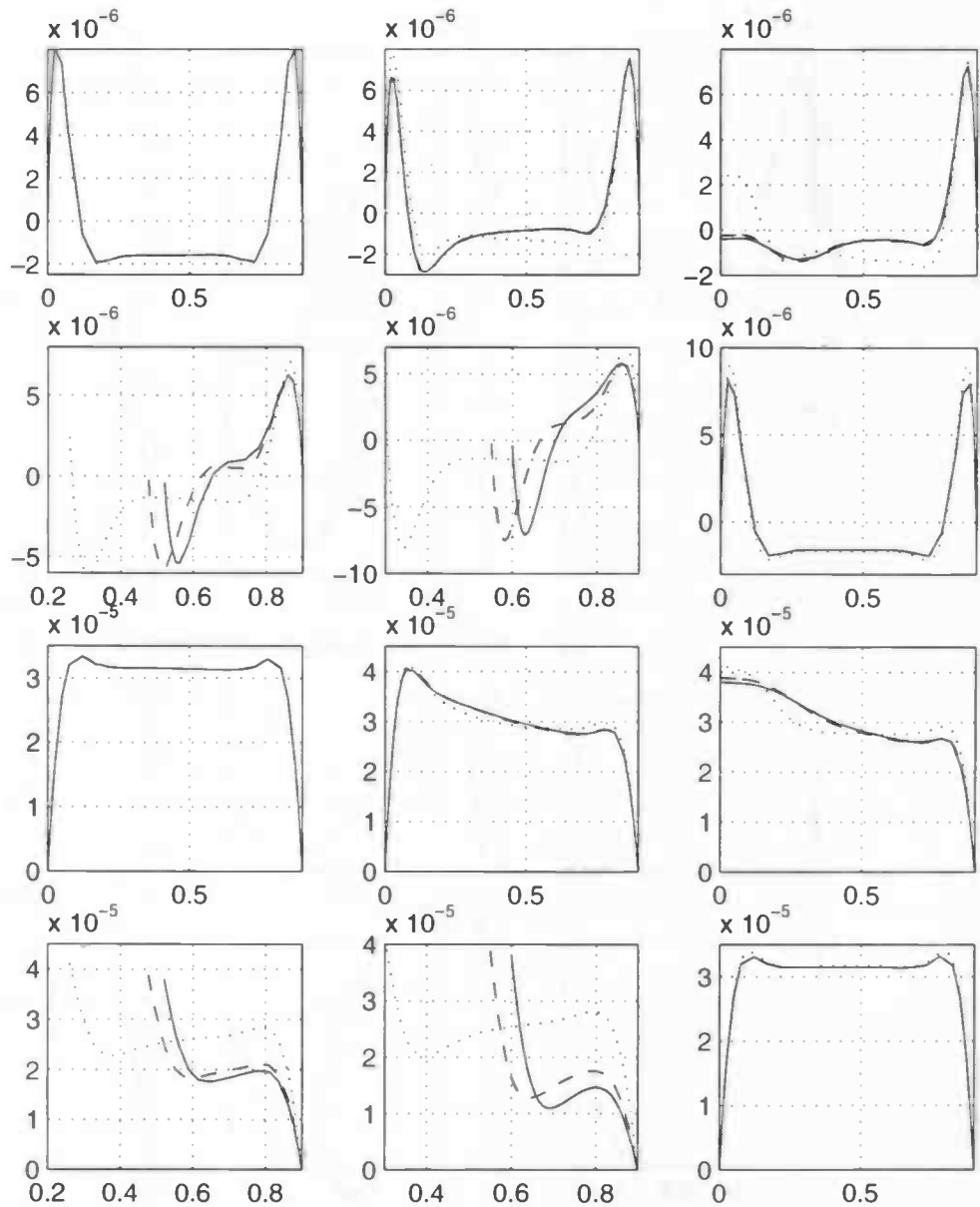


Figure 4.19: The horizontal velocity at the time of zero (pictures a to f) and maximum inflow (pictures g to l) at different cross-sections (see figure 4.4) for $f = 200$ Hz, $r = 0.3$ mm (dotted line), $r = 0.55$ mm (dashed line) and $r = 0.6$ mm (solid line), $n = 32$. In the pictures f and l the solid lines are the approximations and the dotted lines are the Womersley profiles.

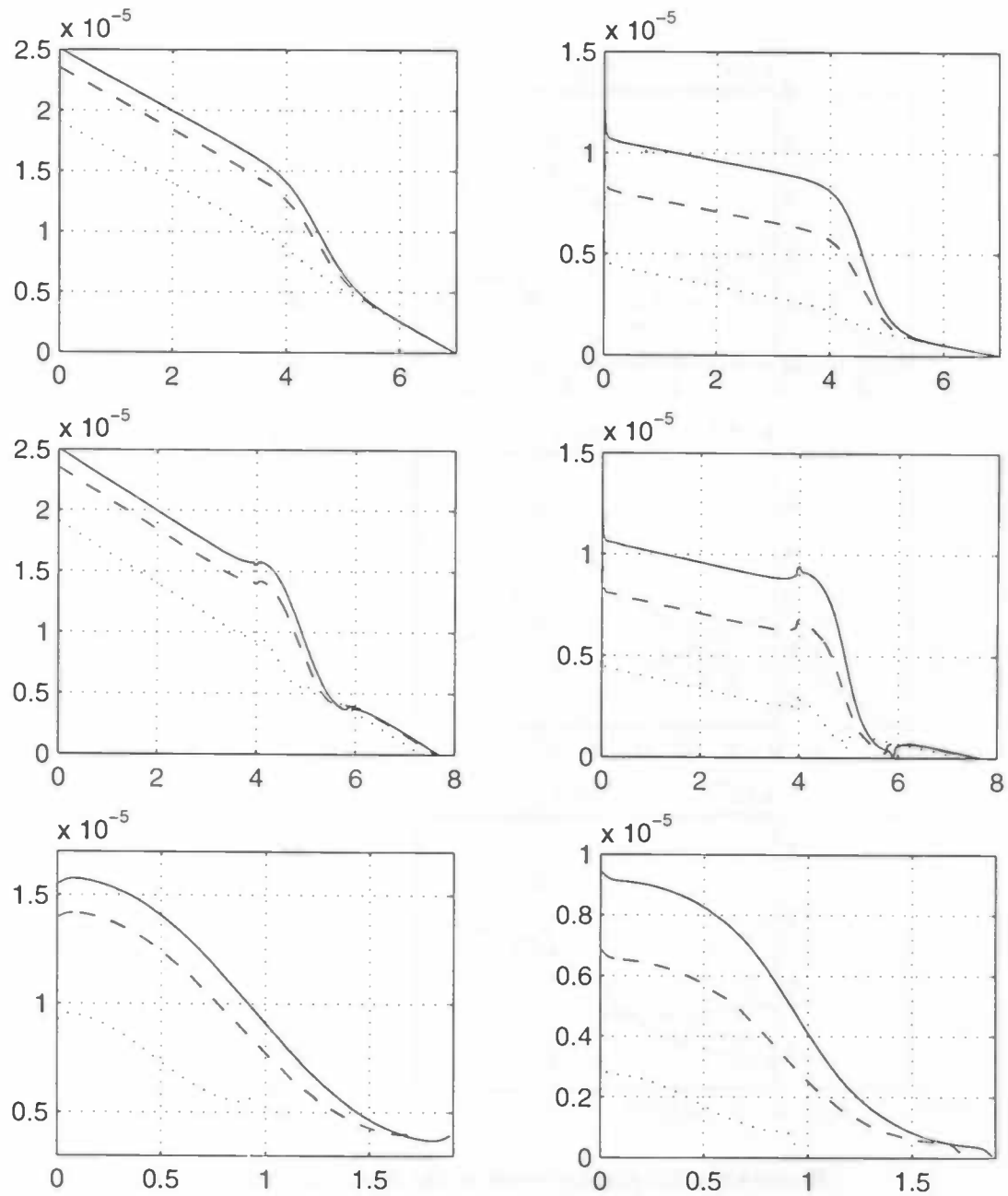


Figure 4.20: The pressure profile at the upper wall (first row), bottom wall (second row) and cupula (third row) for the times of zero (left side) and maximum inflow (right side) for $f = 50$ Hz, $r = 0.3$ mm (dotted line), $r = 0.55$ mm (dashed line) and $r = 0.6$ mm (solid line), $n = 32$.

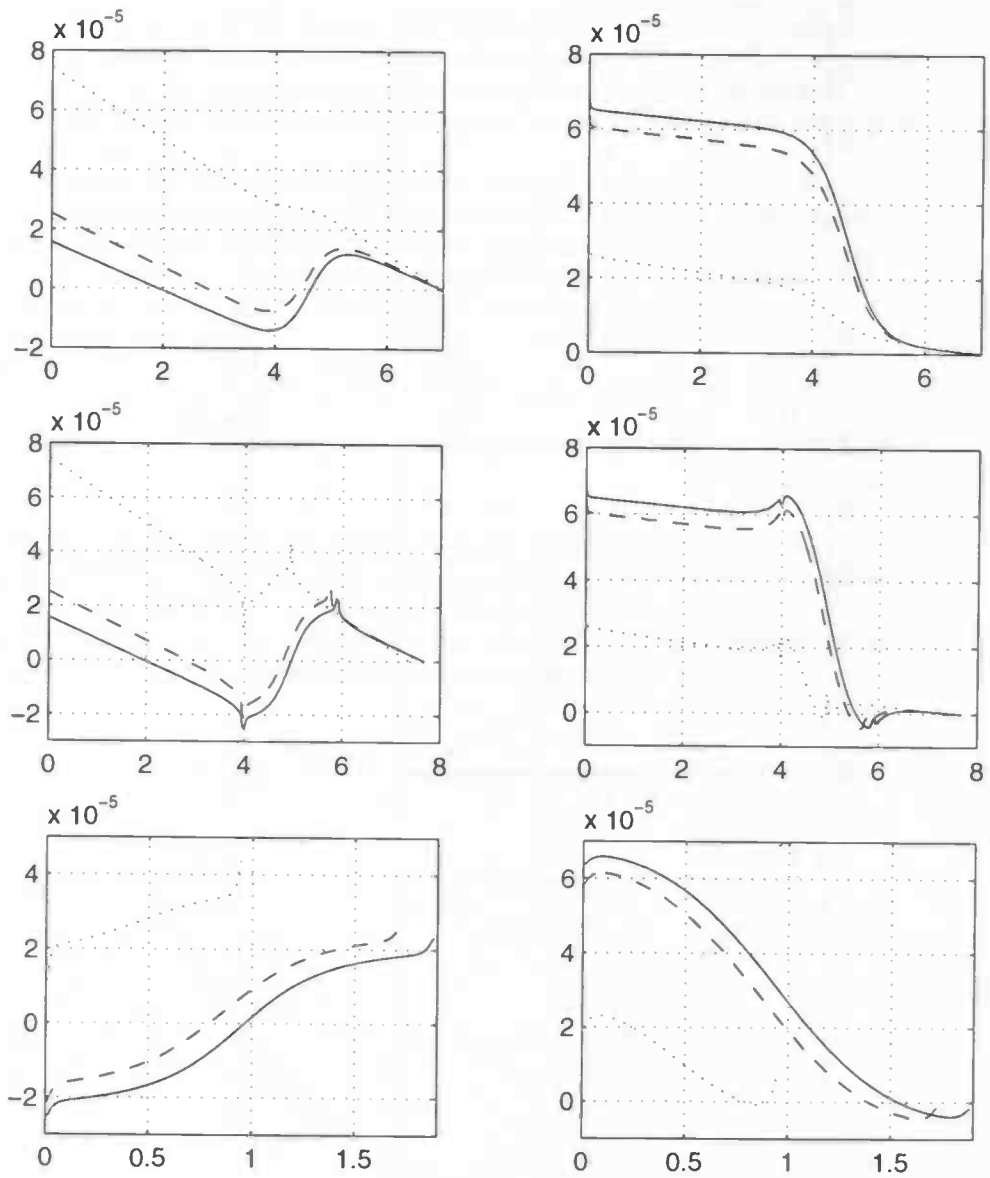


Figure 4.21: The pressure profile at the upper wall (first row), bottom wall (second row) and cupula (third row) for the times of zero (left side) and maximum inflow (right side) for $f = f_{res}$, $r = 0.3$ mm (dotted line), $r = 0.55$ mm (dashed line) and $r = 0.6$ mm (solid line), $n = 32$.

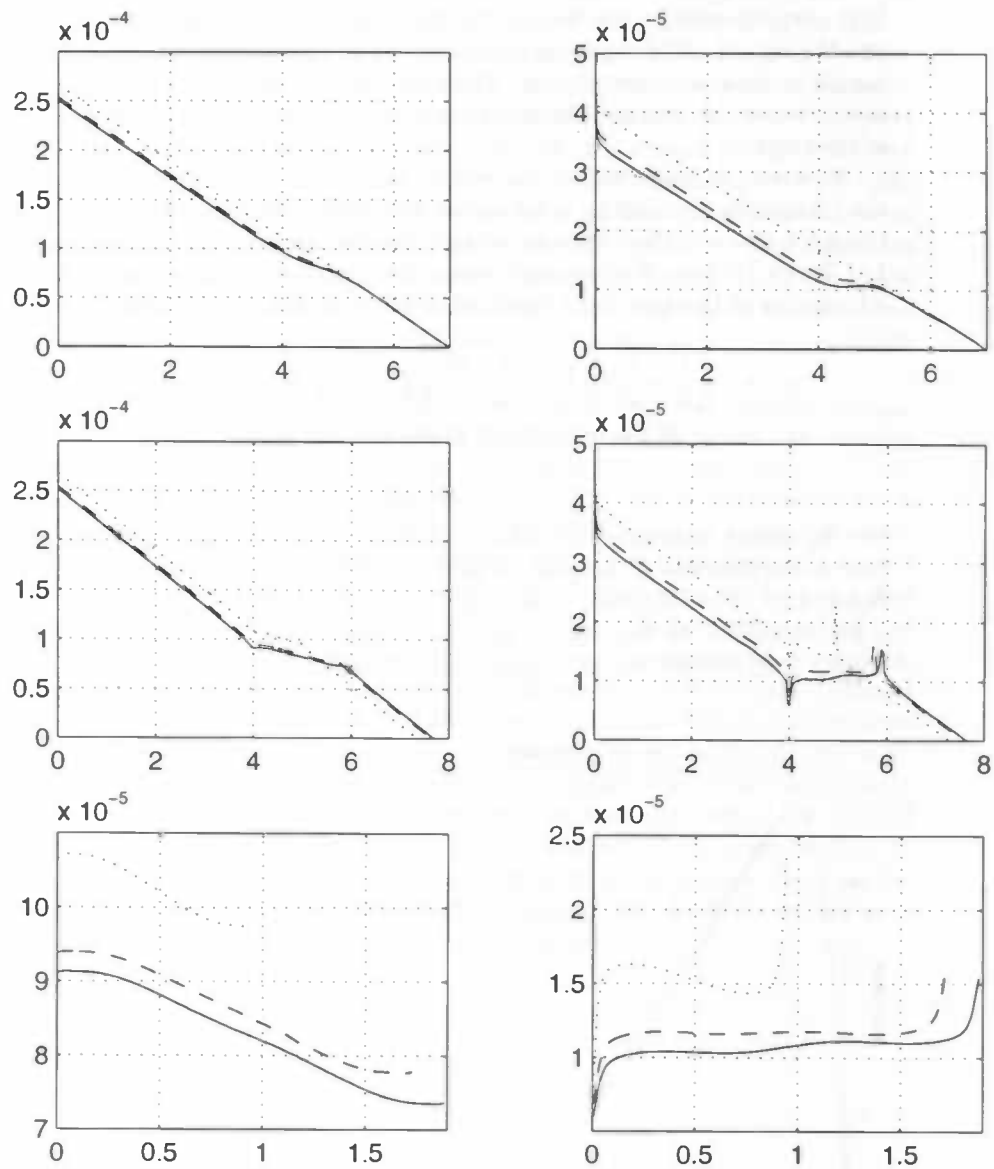


Figure 4.22: The pressure profile at the upper wall (first row), bottom wall (second row) and cupula (third row) for the times of zero (left side) and maximum inflow (right side) for $f = 200$ Hz, $r = 0.3$ mm (dotted line), $r = 0.55$ mm (dashed line) and $r = 0.6$ mm (solid line), $n = 32$.

4.2 The 2D channel with lens

In the experiments by van Netten [10], the upper wall of the channel was removed and the lens of a 40x objective was placed at fixed distances from the top of the cupula to do the measurements. They were always done with a distance of 1.6 mm between the lens and the observed part, for example the top or the bottom of the cupula.

Now we are interested in the results computed with SEPRAN. Because of the complicated geometry, a 2D model was used. The radius of the cupula was taken 0.6 mm and the distances between the lens and the top of the cupula were 1, 1.3 and 1.6 mm. For the area where the cupula meets the bottom wall, the adaptation in the boundary condition is taken at the bottom wall:

$$u = \left(\frac{1}{2} + \frac{1}{2} \cos \left(\frac{\pi(|x| - r)}{\delta} \right) \right) u_{cupula} \text{ for } r \leq |x| \leq r + \delta \quad (4.6)$$

$$u = 0 \text{ at the other parts of the bottom wall} \quad (4.7)$$

$$v = 0 \quad (4.8)$$

On the inflow boundary, the inflow velocity was chosen such that the greatest part of the flux was at the place of the original channel. An example is shown in figure 4.23. The total flux caused by this kind of inflow profiles can be seen as a percentage of the flux caused by a flat inflow profile with maximum velocity. In this way, certain flux percentages can be taken for the inflow.

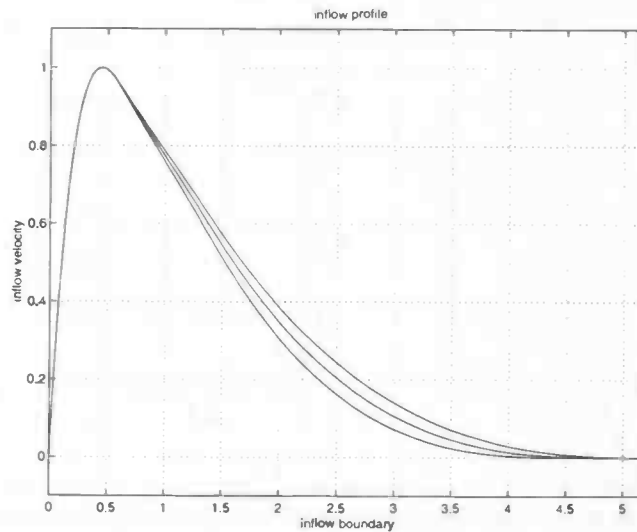


Figure 4.23: Inflow profiles with flux percentage 33.3% for different distances between the lens and the top of the cupula. The maximum velocity is normed at 1.

In the same way as in the 2D channel case, it can be proved that there is an optimum choice of c_{pred} such that the solution does not change much when the time step is decreased. In this section the value of c_{pred} is chosen to be 0.3. Now, let's look at the results for a flux percentage of 50 %, shown in figure 4.24, and a flux percentage of 33.3 %, shown in figure 4.25. The most remarkable fact is the large phase difference for low frequencies, which is at least 20 degrees larger than in the case of the channel. This effect is caused by the geometry at the lefthand side of the cupula. Compared with the axisymmetric case, the phase difference in the case of the channel is at least 20 degrees larger at low frequencies. This is an effect caused by the 2D geometry. The resonance frequency increases if the lens is further away from the cupula. The peak in the amplitude of displacement is only a little bit higher if the lens is nearer to the cupula. Further, the amplitude of displacement depends linearly on the inflow flux.

In figures 4.26, 4.27 and 4.28 the time response of the inflow velocity, u_{cupula} , ξ and F are shown for $f = 50, 110$ and 200 Hz. At 50 Hz a periodic solution is reached within 5 periods. At 110 Hz the amplitudes increase with the time, but after 10 periods this is no longer visible. For $f = 200$ Hz the solution has a capricious character during the first 8 periods, but it tends to a periodic state.

Now, let's look at the effect on the flow when the triangular part of the geometry at the righthand side is removed. This is done with the lens at 1 mm from the top of the cupula. The velocity pictures show the horizontal velocity at some cross-sections and the pressure pictures show the pressure at the cupula. The velocity pictures are again labelled in reading order at the cross sections a) $x=-r$, b) $x=0$, c) $x=0.6$, d) $x=0.7$, e) $x=2.4$ and f) $x=5.5$. These cross-sections are shown in figure 4.29. The velocity pictures are shown in the figures 4.30, 4.31 and 4.32. The pressure pictures are shown in figure 4.33. From the pressure pictures it is clear that the pressure gradient on the cupula stays the same if the geometry at the righthand side is changed. Further, in the velocity pictures there is no difference visible at the cross-sections near the cupula. Even on the cross-section with label e), 1.8 mm on the righthand side from the cupula only little difference is visible, if the geometry is changed.

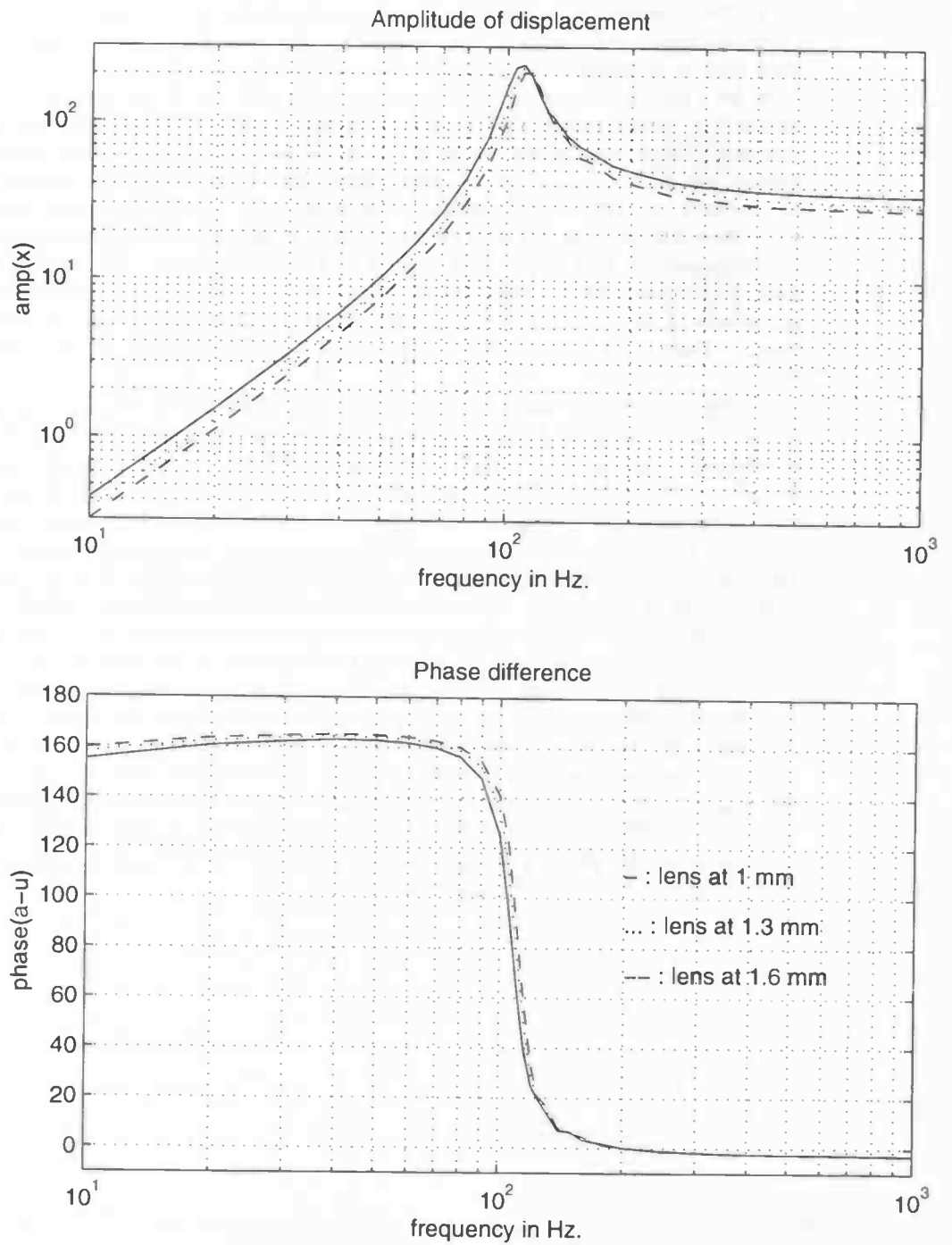


Figure 4.24: Amplitude of displacement and phase difference between inflow velocity and u_{cupula} as function of frequency.

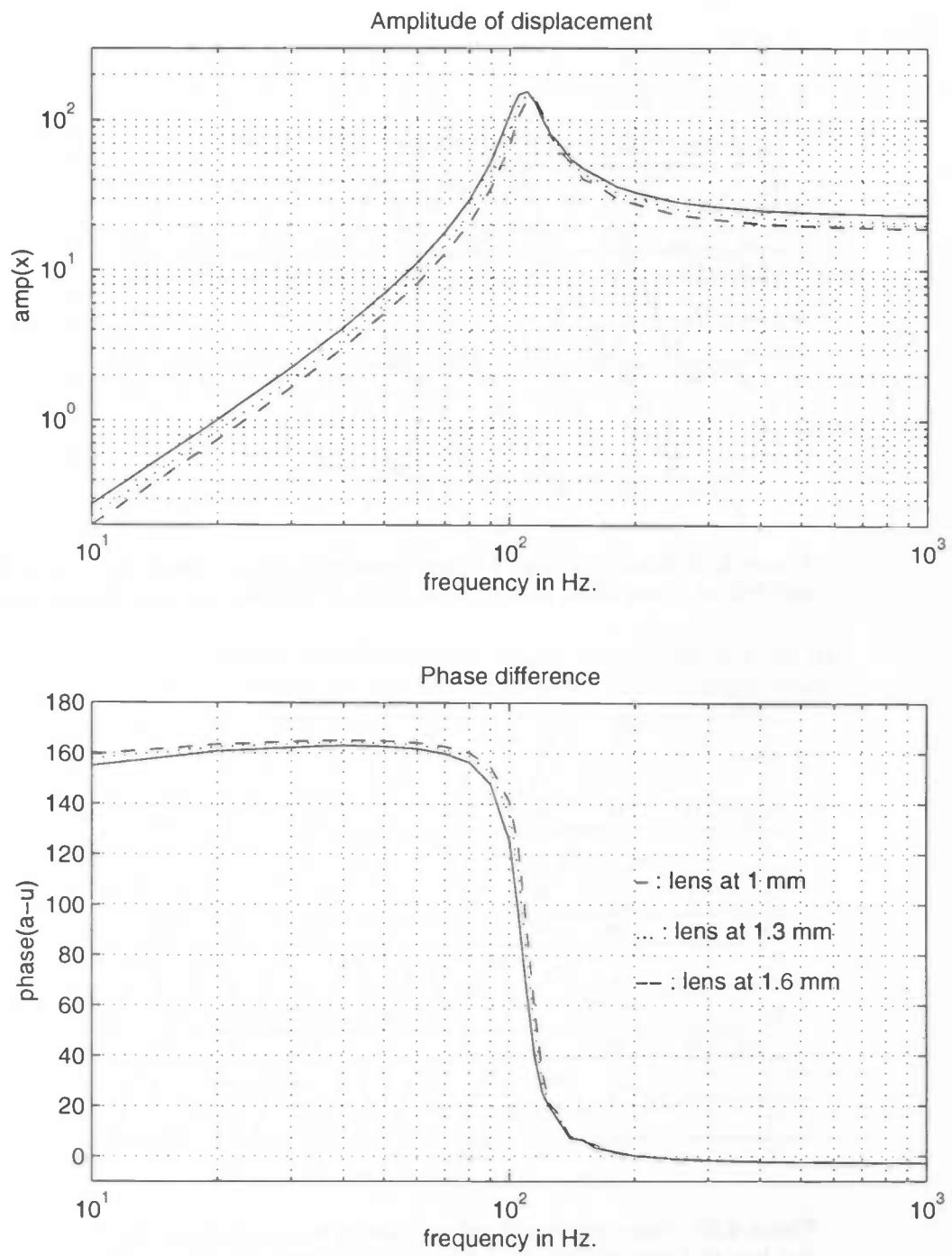


Figure 4.25: Amplitude of displacement and phase difference between inflow velocity and u_{cupula} as function of frequency.

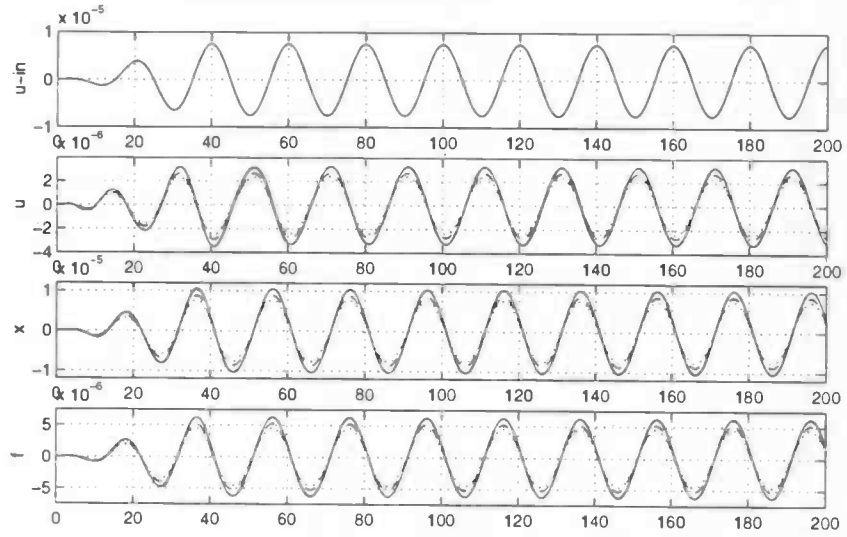


Figure 4.26: Time response of inflow velocity, u_{cupula} , ξ and F for $f = 50$ Hz and lens at 1 mm (solid line), 1.3 mm (dashed line) and 1.6 mm (dotted line).

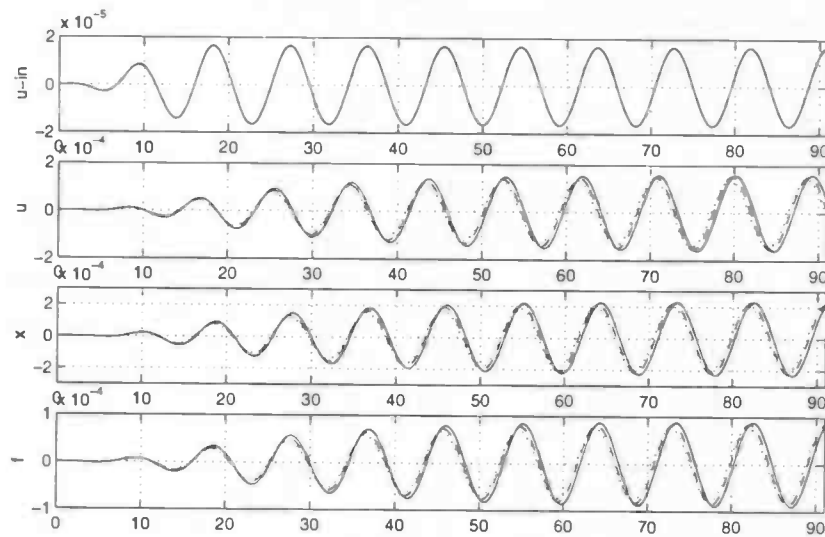


Figure 4.27: Time response of inflow velocity, u_{cupula} , ξ and F for $f = 110$ Hz and lens at 1 mm (solid line), 1.3 mm (dashed line) and 1.6 mm (dotted line).

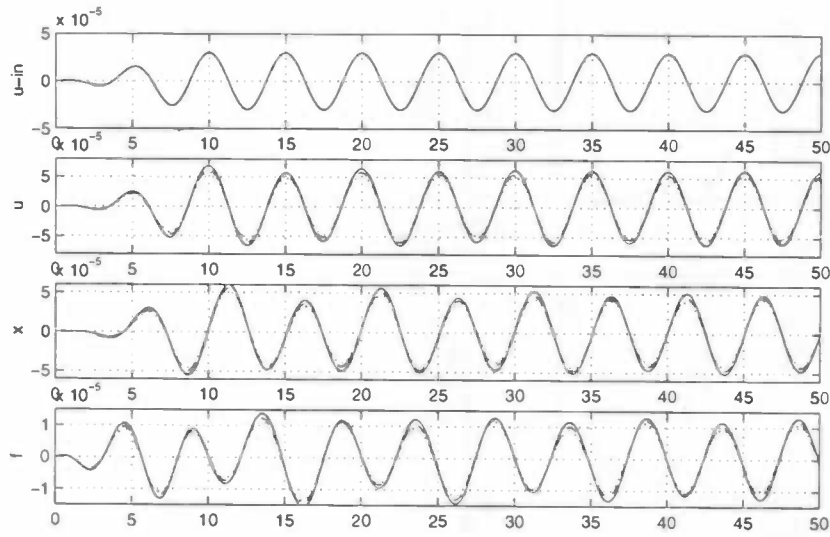


Figure 4.28: Time response of inflow velocity, u_{cupula} , ξ and F for $f = 200$ Hz and lens at 1 mm (solid line), 1.3 mm (dashed line) and 1.6 mm (dotted line).

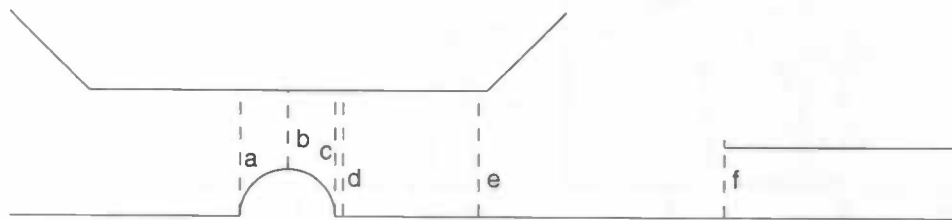


Figure 4.29: The different cross-sections

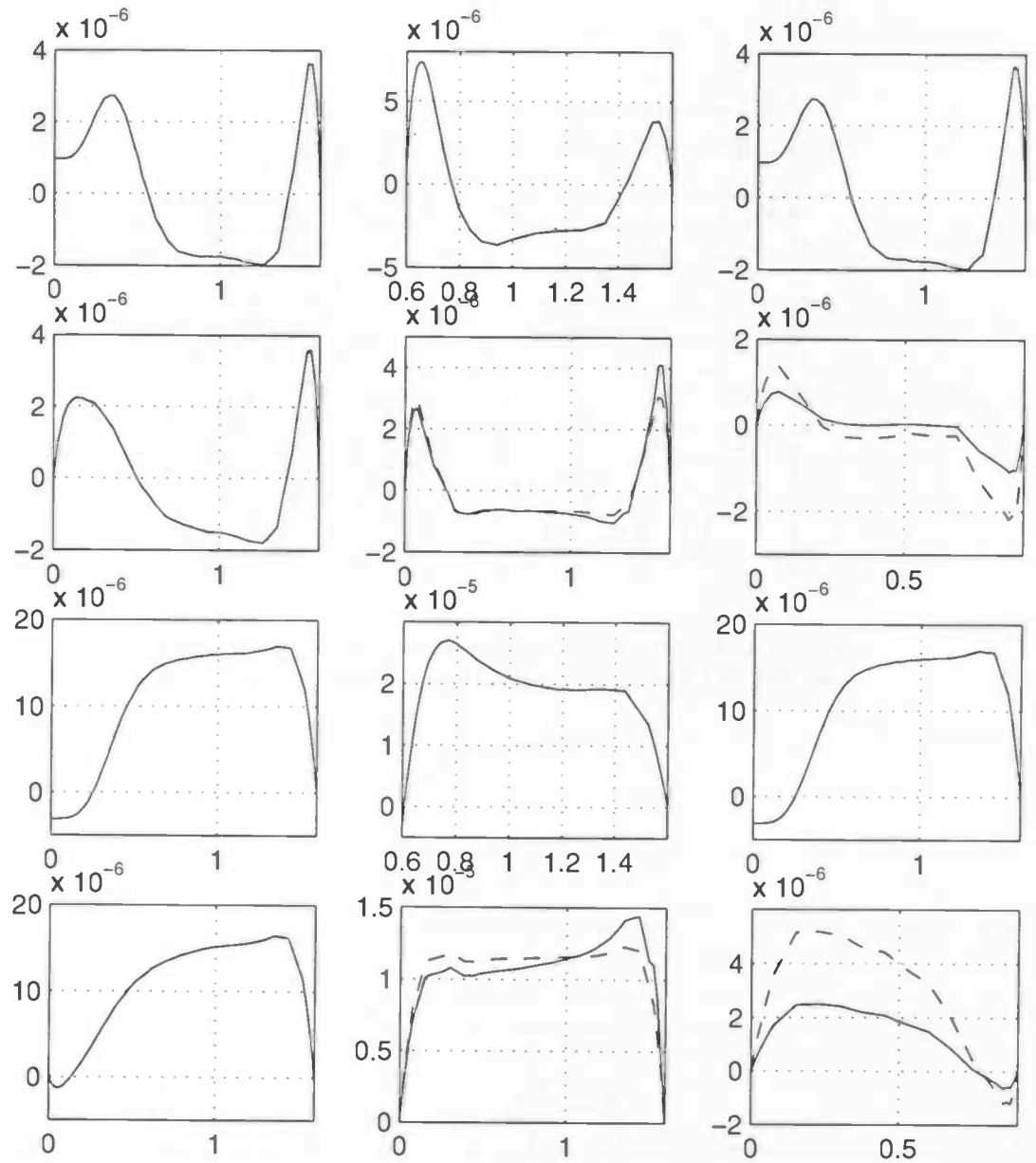


Figure 4.30: Horizontal velocity at the time of zero (pictures a to f) and maximum inflow (pictures g to l) at different cross-sections (see figure 4.29) for $f = 50$ Hz with lens at 1 mm (solid line) and changed geometry (dashed line).

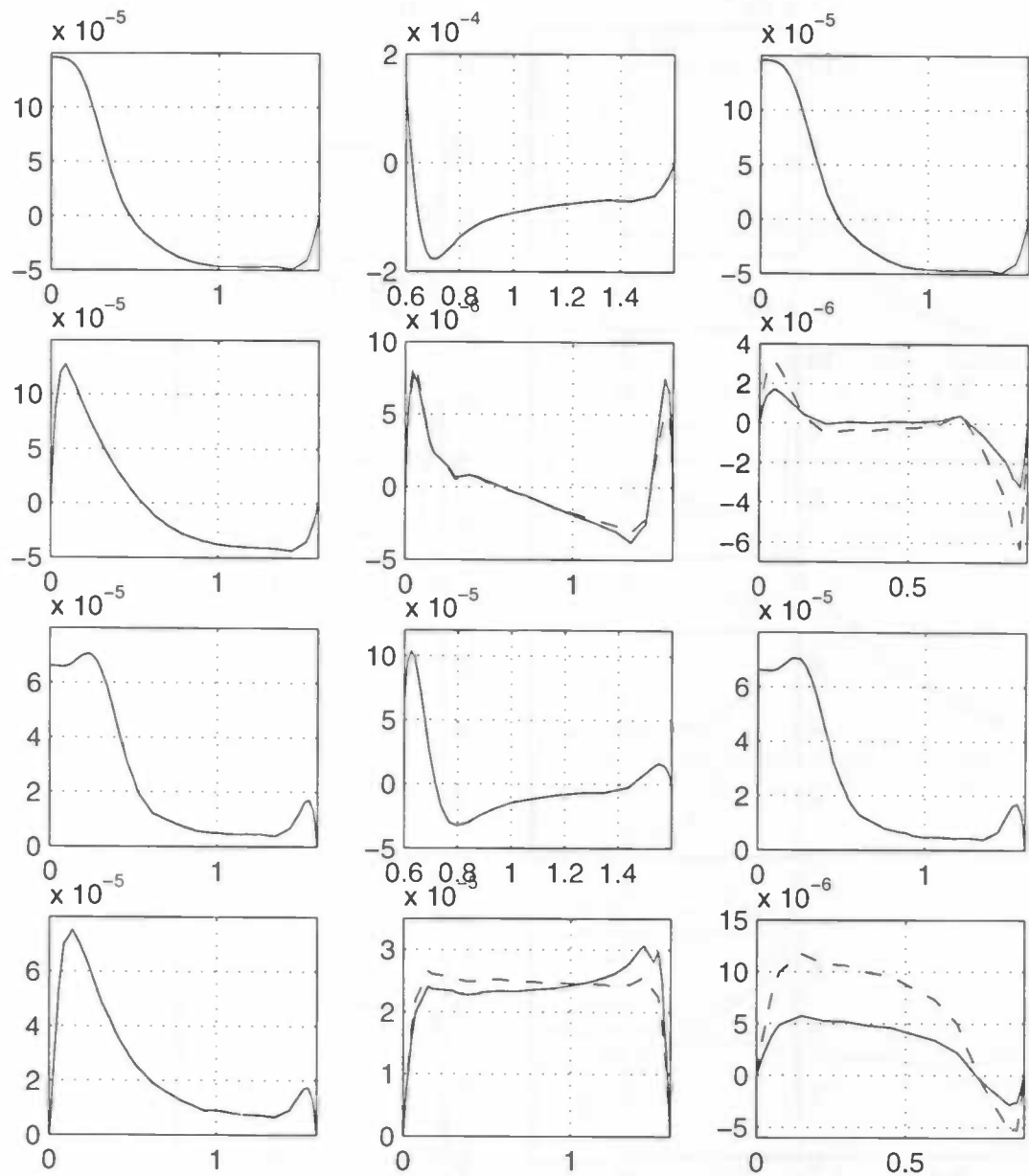


Figure 4.31: Horizontal velocity at the time of zero (pictures a to f) and maximum inflow (pictures g to l) at different cross-sections (see figure 4.29) for $f = 110$ Hz with lens at 1 mm (solid line) and changed geometry (dashed line).

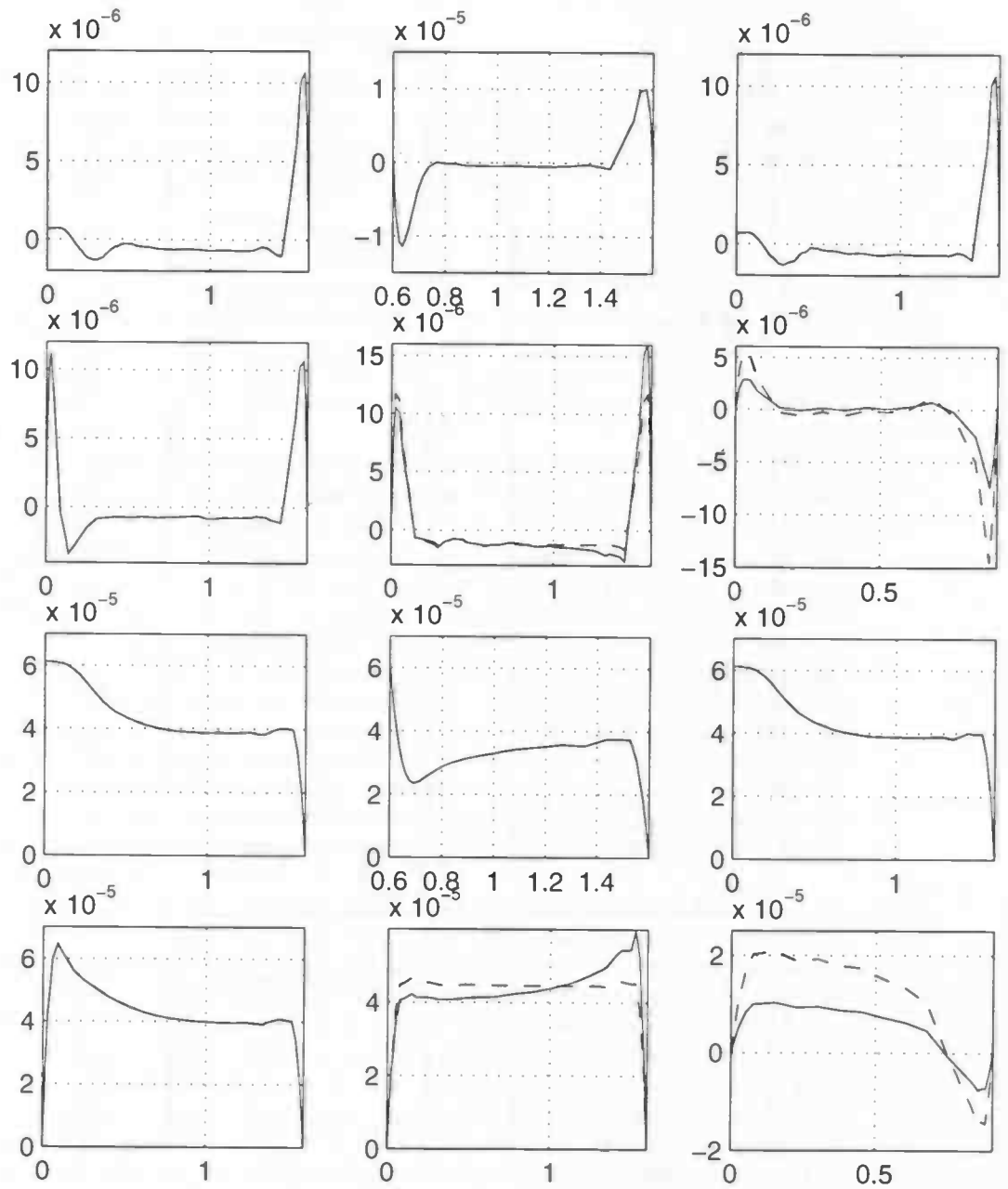


Figure 4.32: Horizontal velocity at the time of zero (pictures a to f) and maximum inflow (pictures g to l) at different cross-sections (see figure 4.29) for $f = 200$ Hz with lens at 1 mm (solid line) and changed geometry (dashed line).

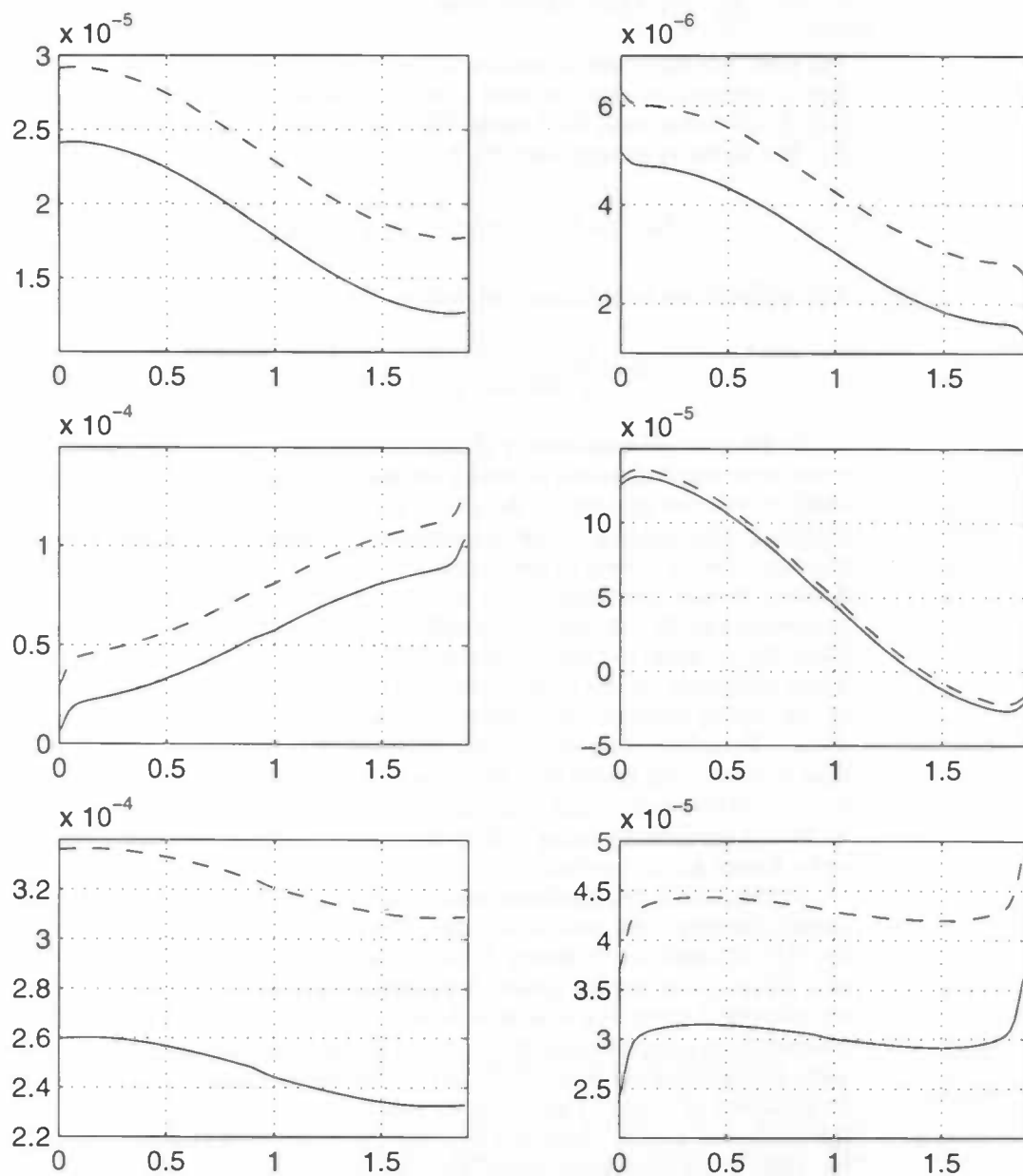


Figure 4.33: Pressure on the cupula for $f = 50$ Hz, f_{res} and 200 Hz with the lens at 1 mm (solid line) and changed geometry (dashed line).

4.3 The axisymmetric geometry with nonlinearity in the stiffness

Till now, the equations of motion of the cupula were considered to be linear. But in reality they are nonlinear, caused by a nonlinear term in the stiffness [12]. In the linear case, the force on the cupula caused by the stiffness was taken Sx . But in the nonlinear case, the force becomes:

$$F_s(x) = Sx - \frac{k_1}{e^{-k_2(x-x_0)} + 1} + \frac{k_1}{e^{-k_2(-x-x_0)} + 1} \quad (4.9)$$

The stiffness can be calculated by taking $\frac{dF_s}{dx}$, giving the following formula:

$$S - \frac{k_1 k_2 e^{-k_2(x-x_0)}}{(e^{-k_2(x-x_0)} + 1)^2} - \frac{k_1 k_2 e^{-k_2(-x-x_0)}}{(e^{-k_2(-x-x_0)} + 1)^2} \quad (4.10)$$

To see how the nonlinearity changes the motions of the cupula, only a few extra terms must be added to the equations of motion of the cupula. So, numerically there is no problem to do this, if the number of time steps per period is sufficient. But introducing the nonlinearity in an analytical model means that the equations of motion of the cupula can no longer be solved in the frequency domain. In the linear case the cupula moves with one frequency ω , so the displacement can be supposed to be $x(t) = x_0 e^{i\omega t}$. Substituting this in the fluid force, F_{fluid} , leads to time-independent equations for the motion of the cupula. These equations can be solved exactly [11]. In the nonlinear case, the motion of the cupula contains more frequencies, so the time can not be eliminated in F_{fluid} . Therefore, the equations of motion of the cupula must be solved in the time domain. This means that in the analytical model, F_{fluid} must be rewritten in terms of first and second order time derivatives. After this, the equations can be solved numerically using a time-integration method, for example a fourth order Runge Kutta method.

To check both the nonlinear analytical model and the SEPRAN model, we simply compare them with each other. The analytical model, used by van Netten [11], is based on the theory of Stokes flows, where the cupula is considered as a sphere in an infinite space. This means that for a proper comparison, in the numerical model the wall must be at a large distance from the cupula. The computations are done with the wall at a distance of 4 mm from the symmetry wall. It appears from figure 4.36 that taking the dynamical viscosity $4.5 \cdot 10^{-3}$ Pa.s instead of $5 \cdot 10^{-3}$ Pa.s, used by van Netten, results in a better fit with the analytical model. This is a well-known effect [6]: introducing a wall has the same effect on the motion of the cupula as increasing the viscosity. The radius of the cupula was taken $3 \cdot 10^{-4}$ mm, the density of the cupula and the fluid 1000 kg/m^3 and S , the stiffness of the cupula in the linear case, 0.129 N/m . The three parameters in the function $F_s(x)$ were chosen as $k_1 = 10^{-8} \text{ N}$, $k_2 = 2.44 \cdot 10^6 \frac{1}{\text{m}}$, $x_0 = 100 \text{ nm}$. This means that the minimum of the stiffness is reached when the amplitude of displacement is 100 nm. A plot of the stiffness

is shown in figure 4.35. The value of k_1 is the difference between $F_s(x)$ and Sx at infinity. A plot of $F_s(x)$ is shown in figure 4.34. The results of the linear case with $a = 24$ nm, shown in figure 4.36 lead to a resonance frequency of about 120 Hz.

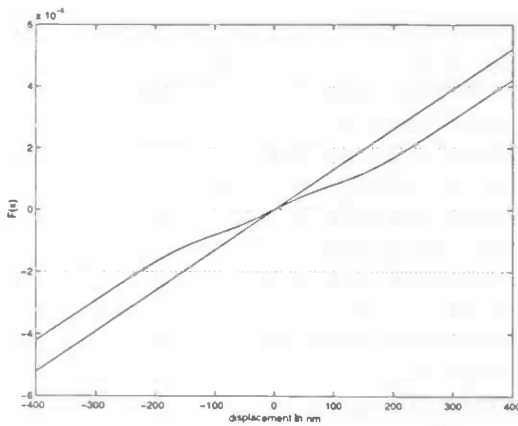


Figure 4.34: Force on the cupula caused by the stiffness as function of ξ

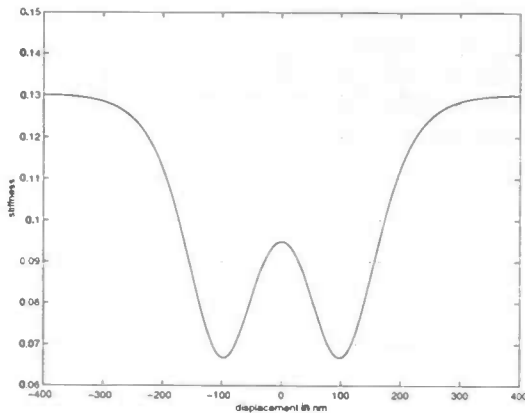


Figure 4.35: Stiffness as function of amplitude of displacement

Now, consider the nonlinear case using SEPRAN. To compute the amplitude of displacement and the phase difference, Fast Fourier Transforms are used. The amplitude of displacement follows from $\sqrt{\text{real}(FT)^2 + \text{imag}(FT)^2}$ and the phase difference follows from $\arctan\left(\frac{\text{imag}(FT)}{\text{real}(FT)}\right)$. The computed amplitude of displacement and phase difference were based on the last four periods, so 128 datapoints were taken in the Fourier transforms. The results with different inflow displacements together with the nonlinear analytical solutions (unpublished) are shown

in figure 4.37. In the plots only little difference is visible between the SEPRAN results and the analytical results. At low frequencies the phase difference of the analytical model is about 5 degrees larger than the SEPRAN results. The largest difference in the amplitude is near f_{res} . Further, we see that the resonance frequency decreases to about 90 Hz when the inflow amplitude is increased to 96 nm and then it increases when the inflow amplitude is further increased. When the frequency is above ± 400 Hz, the phase difference becomes slightly negative. In the analytical model the phase difference goes to zero for high frequencies. For low frequencies as well as for high frequencies, the phase difference becomes eventually the same for all different inflow amplitudes.

It is also interesting to examine the difference between the linear and nonlinear case. Therefore, three frequencies are taken with approximately the same amplitude of displacement (200 nm). The dashed lines in the figures 4.38, 4.39 and 4.40 are the linear cases and the solid lines are the nonlinear cases. The figures show the plots of the inflow velocity, the velocity of the cupula, the displacement of the cupula, and the force on the cupula for the linear and nonlinear case. Also, the difference between the linear and nonlinear case for u_{cupula} , ξ and F are shown. It is clear that the most significant distortion occurs at low frequencies. For high frequencies no distortion is visible². The distortion is best seen in the time response of the velocity instead of the displacement. This is obvious since the velocity is the derivative of the displacement. So, in Fourier analysis, the velocity components are the displacements components multiplied by $i\omega$. The distortion in the displacement can better be seen by plotting the Fourier components for one stimulus frequency. In the figures 4.41, 4.42 and 4.43 the Fourier components for the six different inflow amplitudes are shown. The dominant component is at the stimulus frequency and all the others are harmonics. The conclusion that the most distortion occurs at low frequencies can be drawn again.

²Note that in this case the difference between the linear and nonlinear case is not visible when they are plotted in one picture

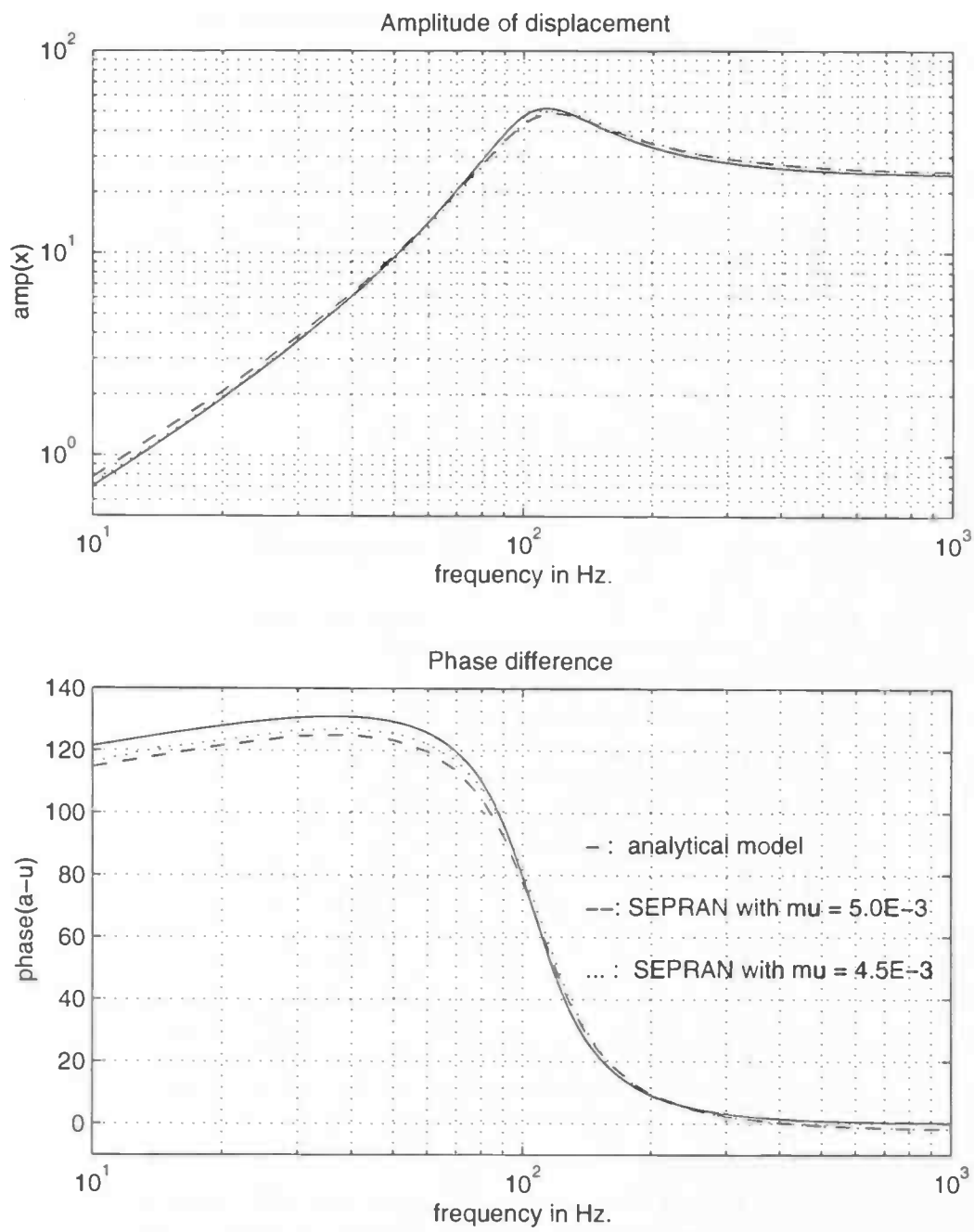


Figure 4.36: Amplitude of displacement and phase difference with $\mu = 5 \cdot 10^{-3}$ Pa.s (dashed line) and $4.5 \cdot 10^{-3}$ Pa.s (dotted line), compared with the linear analytical model (solid line) used by van Netten.

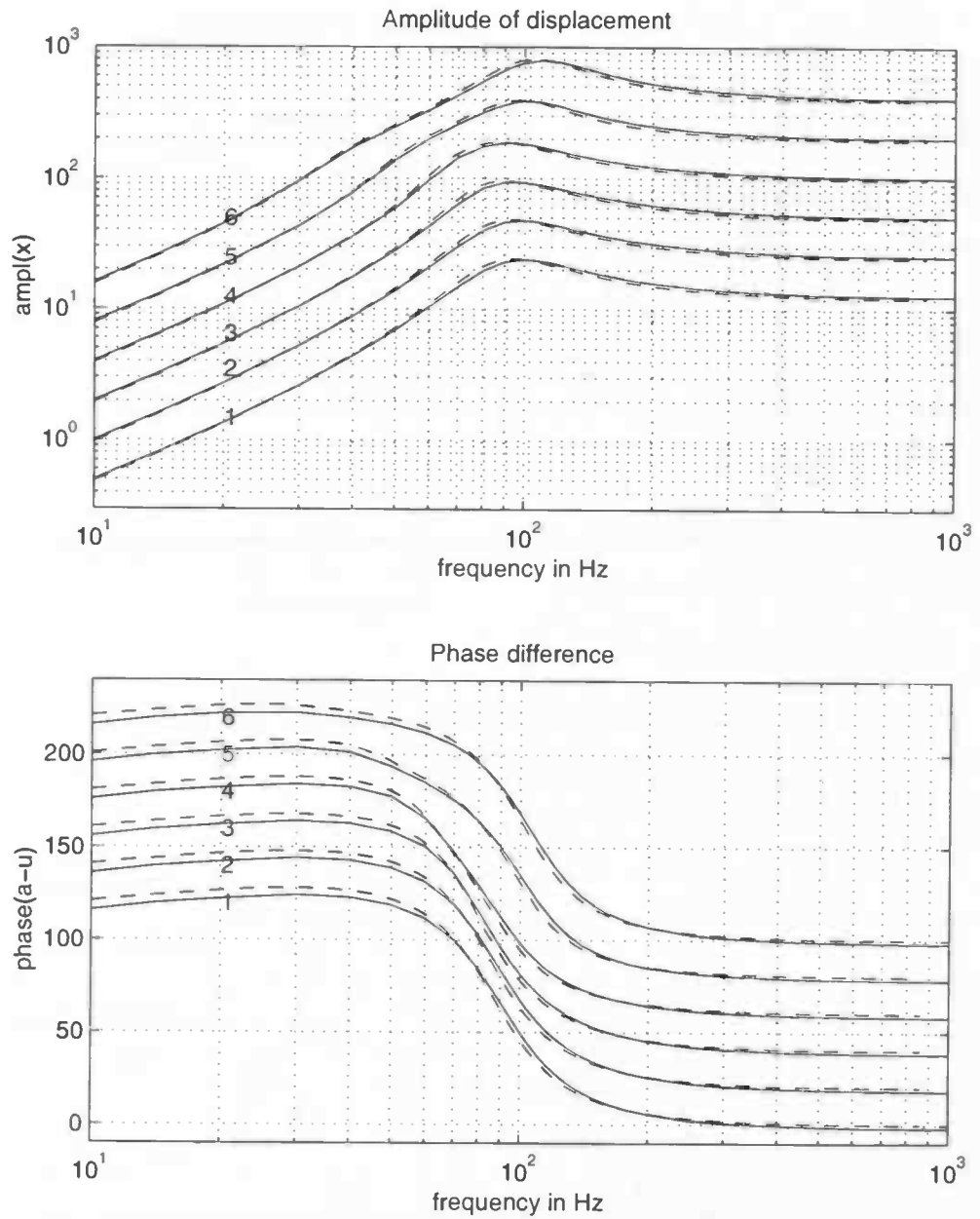


Figure 4.37: Amplitude of displacement and phase difference with different inflow displacements: 1=12nm, 2=24nm, 3=48nm, 4=96nm, 5=192nm, 6=384nm. The phase curves are offset by 0,20,40,60,80 and 100 degrees for case 1 to 6 respectively, in order to improve readability. The solid lines are the SEPRAN results and the dashed lines are the nonlinear analytical results obtained by van Netten.

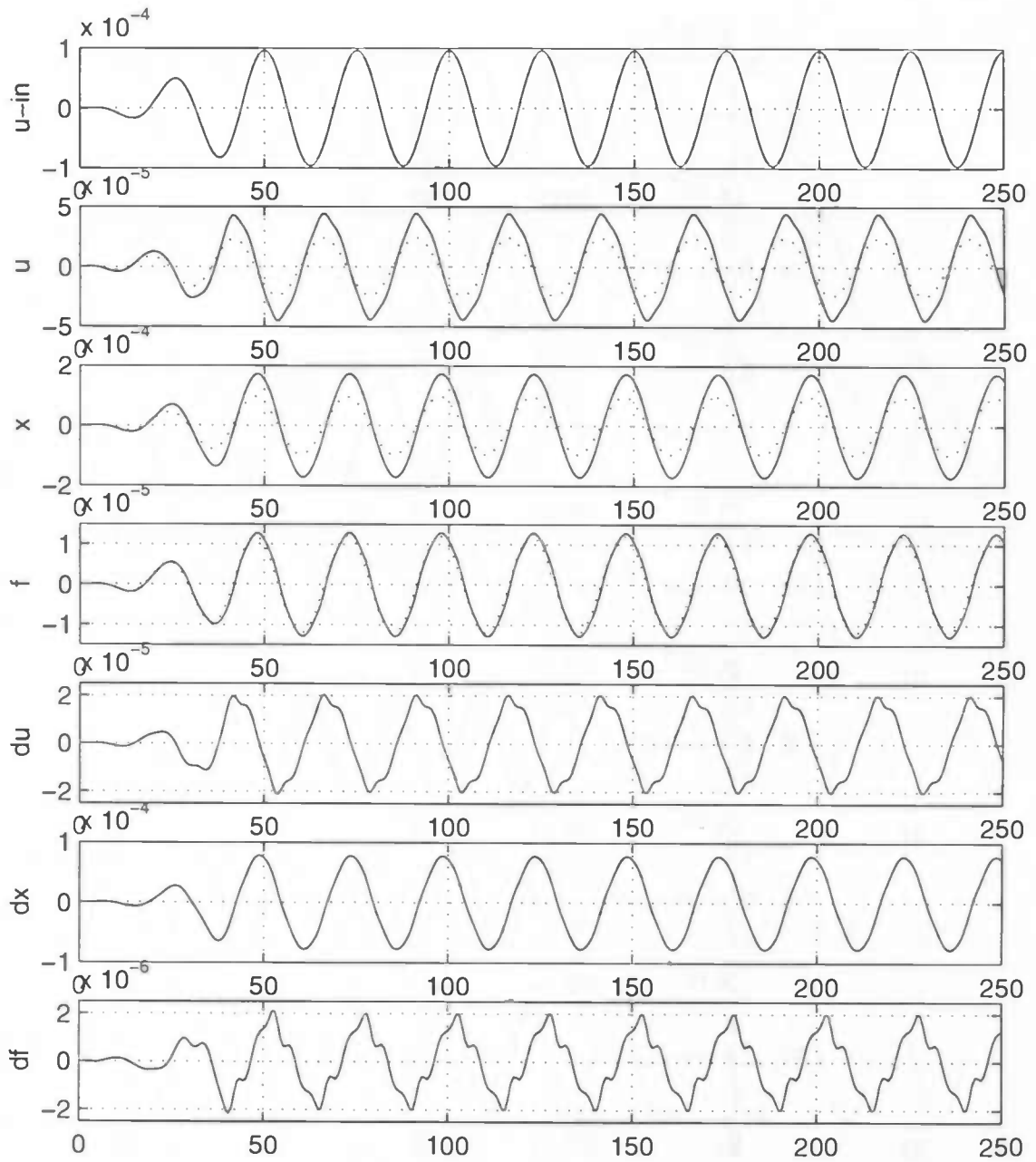


Figure 4.38: Time response of inflow velocity, u_{cupula} , ξ , F (solid line: nonlinear case, dotted line: linear case) and also the difference between the linear and nonlinear case for u_{cupula} , ξ , F . $f = 40$ Hz and inflow displacement is 384 nm

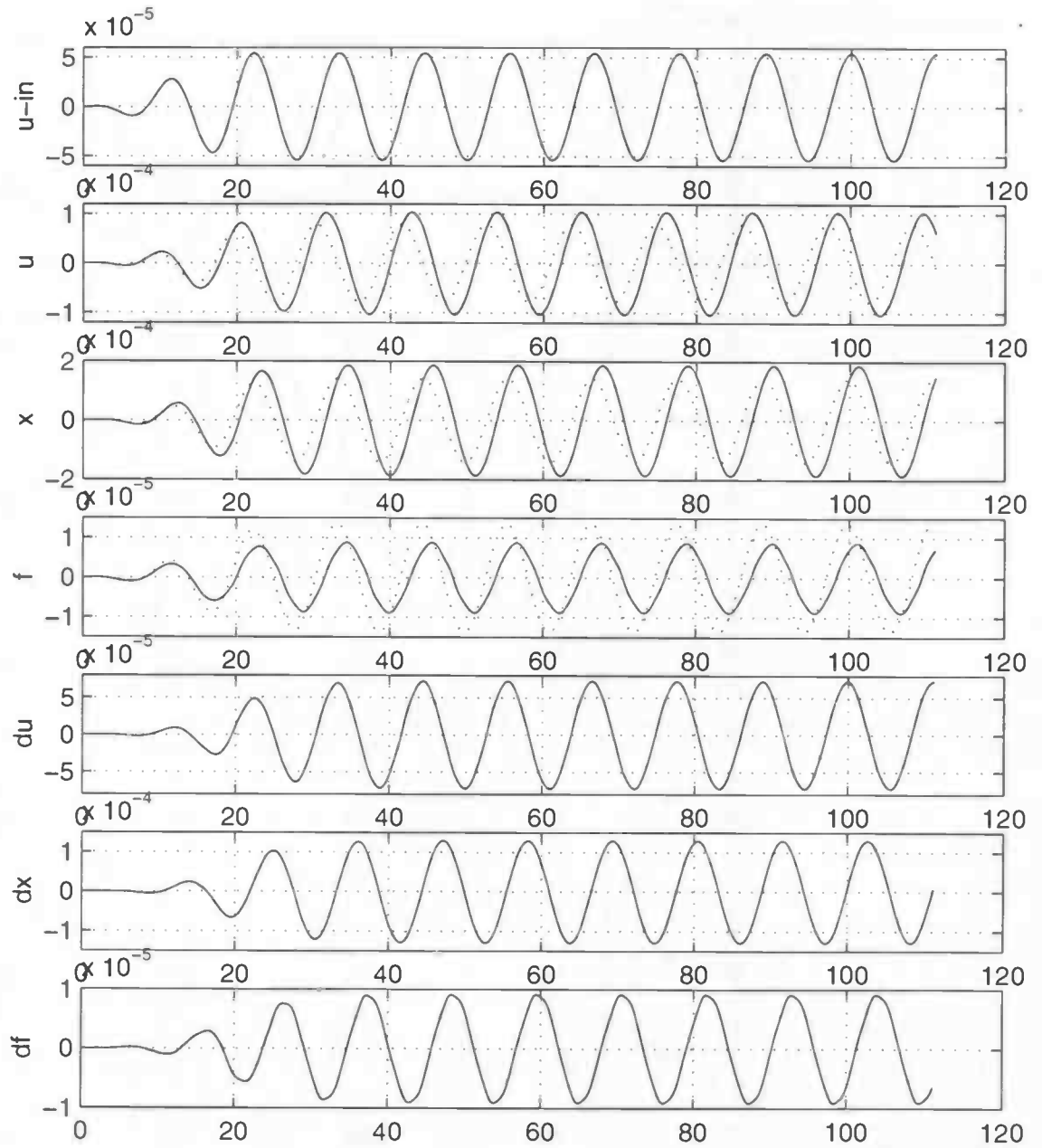


Figure 4.39: Time response of inflow velocity, u_{cupula} , ξ , F (solid line: nonlinear case, dotted line: linear case) and also the difference between the linear and nonlinear case for u_{cupula} , ξ , F . $f = 90$ Hz and inflow displacement is 96 nm

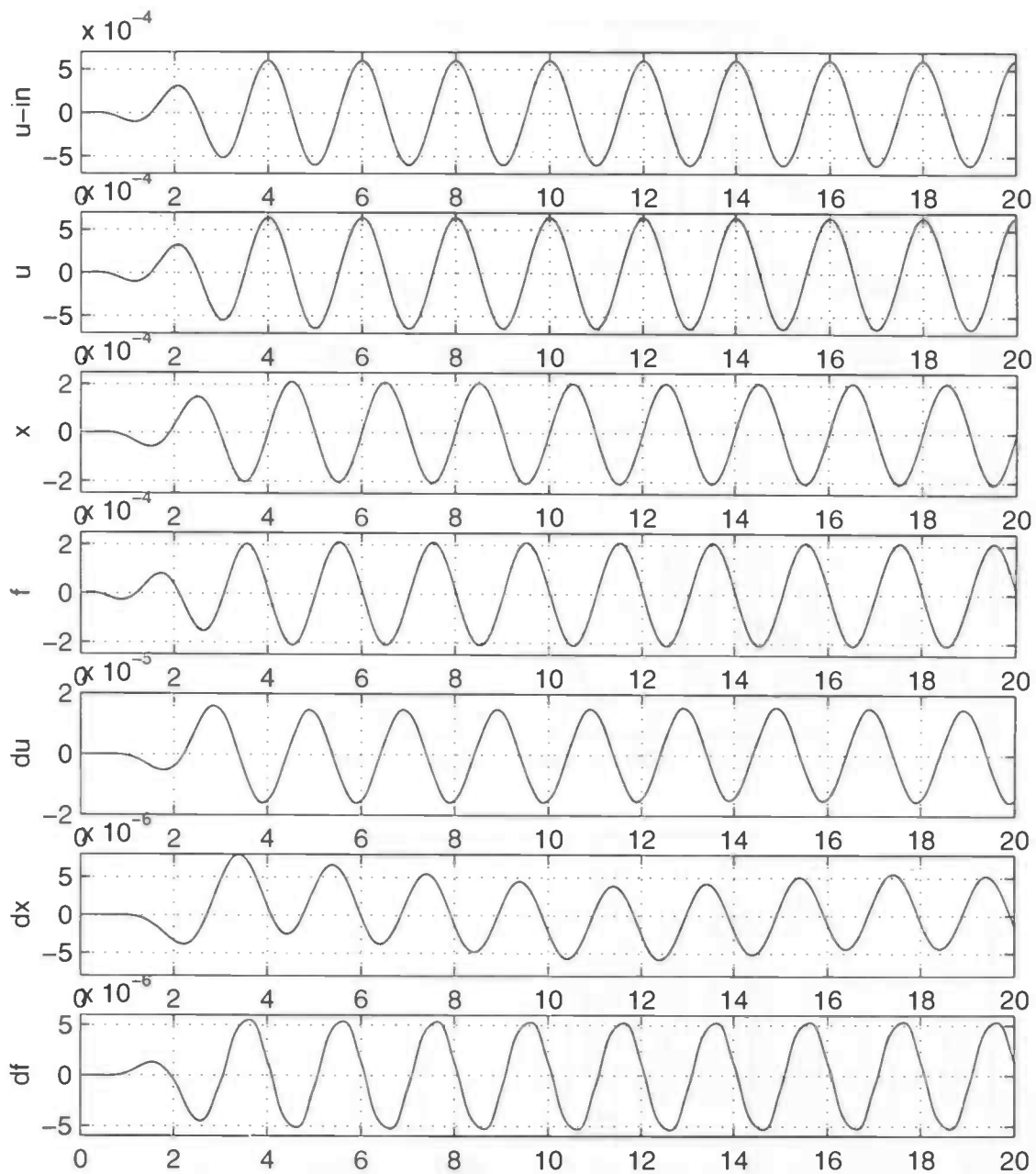


Figure 4.40: Time response of inflow velocity, u_{cupula} , ξ , F (solid line: nonlinear case, dotted line: linear case) and also the difference between the linear and nonlinear case for u_{cupula} , ξ , F . $f=500$ Hz and inflow displacement is 192 nm

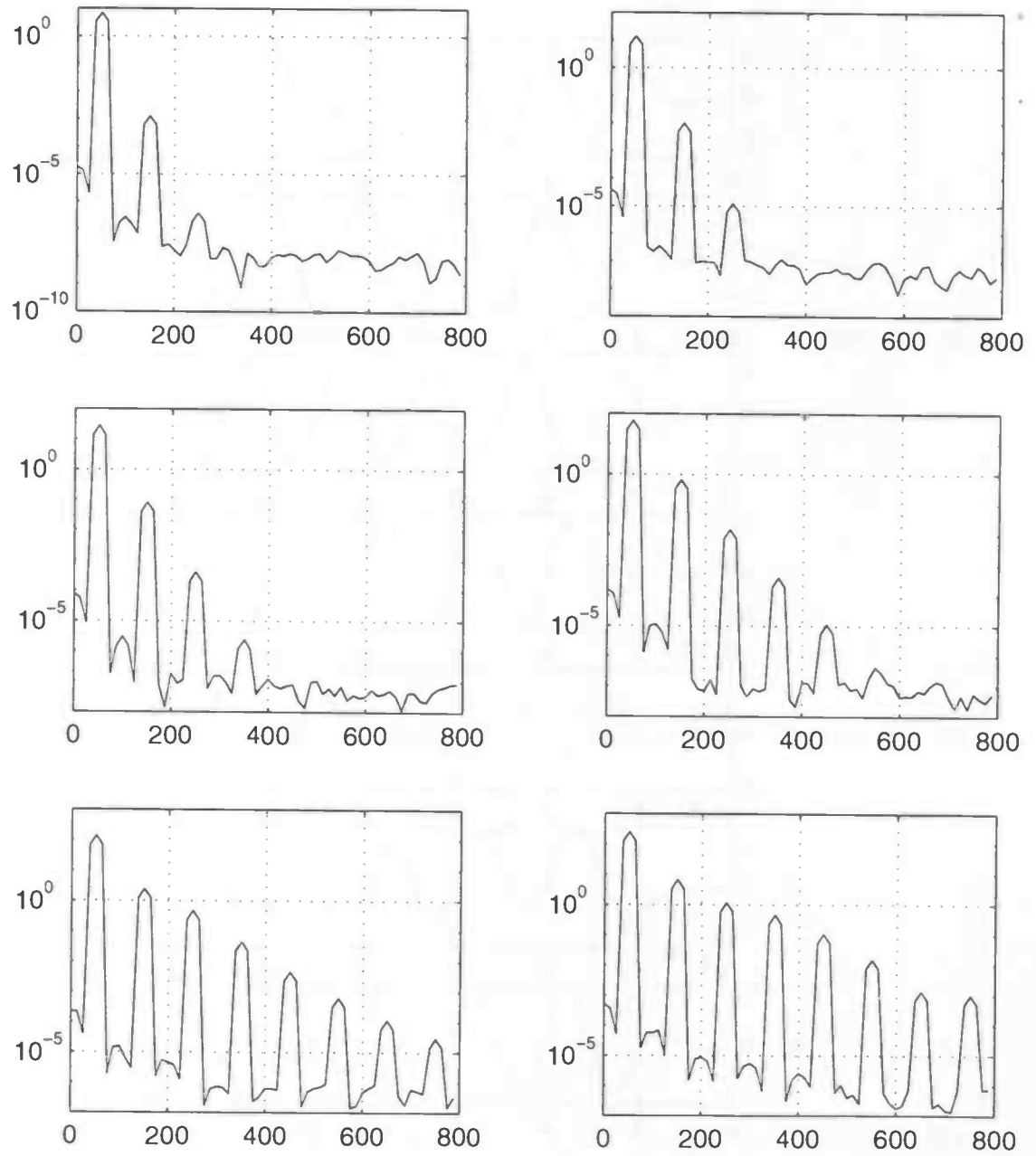


Figure 4.41: Fourier components for $f = 50$ Hz. and inflow displacement 12,24,48,96,192, 384 nm.

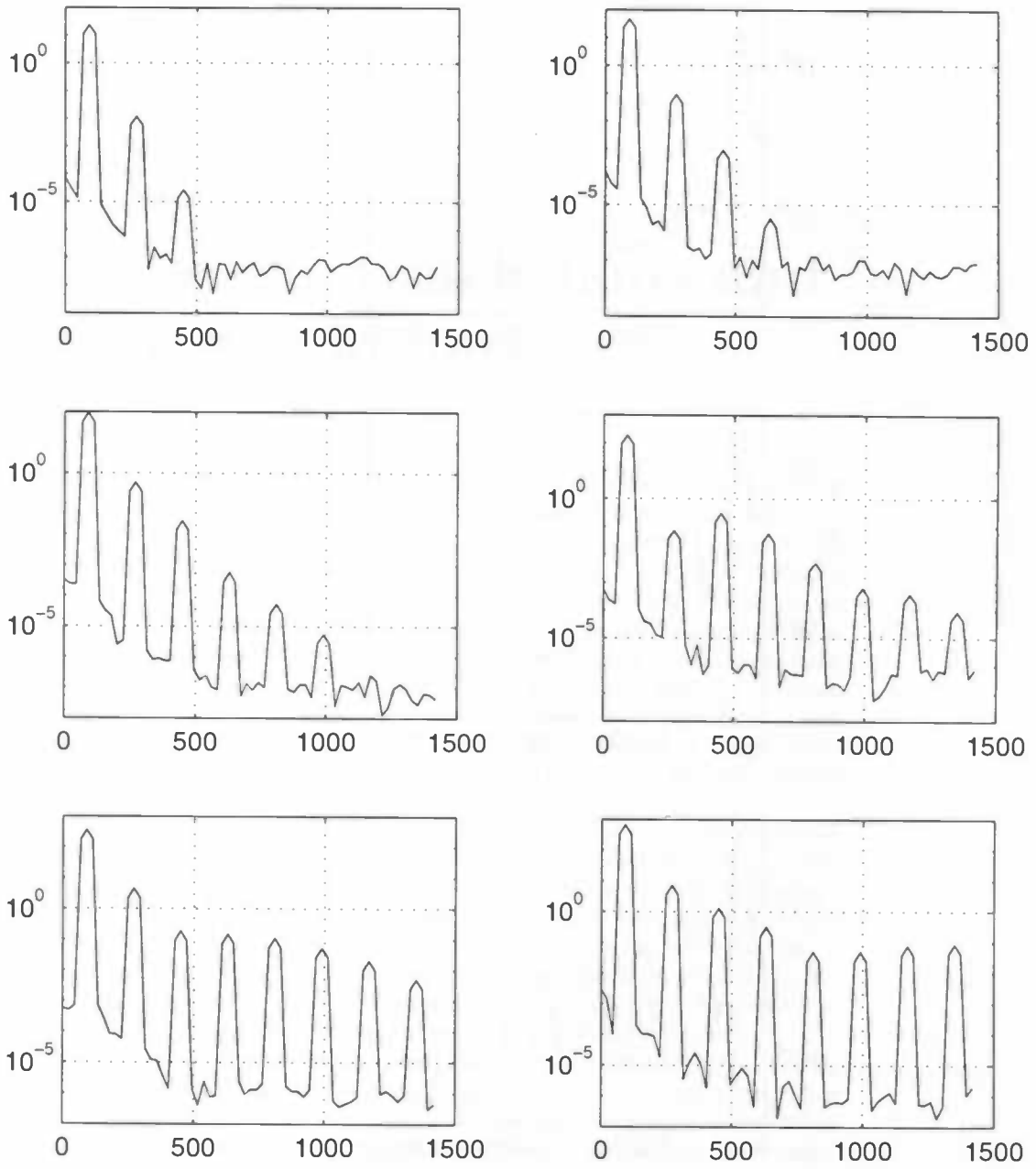


Figure 4.42: Fourier components for $f = 90$ Hz. and inflow displacement 12, 24, 48, 96, 192, 384 nm.

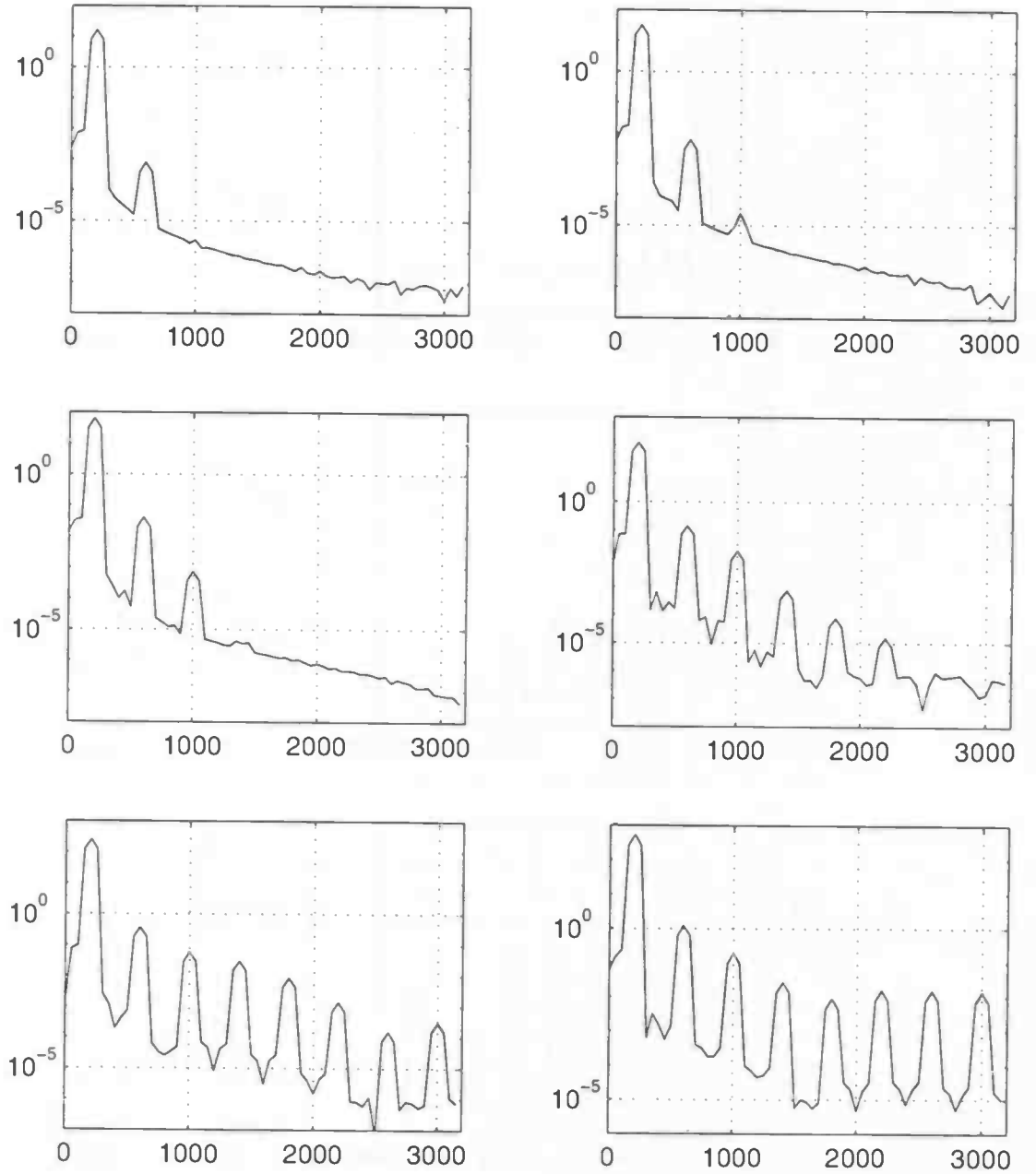


Figure 4.43: Fourier components for $f = 200$ Hz. and inflow displacement 12,24,48,96,192, 384 nm.

Chapter 5

Discussion, conclusions and recommendations

In the 2D channel case, useful computations with an enlarged cupula were only possible when the coefficients of the time-integration method for the equations of motion were changed. There seems to be an optimum choice of c_{pred} at which the solution does not change much when the time step is decreased. This choice can be taken the same for all frequencies and is determined by the choice at f_{res} . The optimum value can be found at other radii by keeping u_{cupula} constant after the first time step. When the cupula is enlarged to the value found in the experiments, some remarkable effects appear at frequencies near f_{res} : strong backward flow above the cupula and a strong reverse pressure gradient in the area of the cupula at the time of zero inflow. The accuracy of the solution could not be tested, because there is no analytical solution to this geometrical situation.

In the 2D model where the lens is used, not much difference occurs compared with the 2D channel case. The most important effect, caused by the lens, is the larger phase difference at low frequencies. When the triangular part of the fluid at the right hand side of the cupula is removed, no effect is visible in the motion of the cupula. A geometry with lens is very suitable to compare the results with the experimental data. If it is possible to do computations with a full 3D model, for instance with ComFlo, the computed motions of the cupula can be compared with the experimental values to test the numerical model.

When the stiffness is nonlinear, most distortion appears at low frequencies as expected. The analytical model used by van Netten gives results which agree closely with the SEPRAN results in the nonlinear case, indicating the usability of both of these models to investigate the effects of nonlinearity on cupular motion and fluid flow. Even at frequencies near the resonance frequency, the amplitudes of displacement differ only a few percents from each other. The main difference is the slightly larger phase difference at low frequencies in the analytical model.

Bibliography

- [1] K.E. Atkinson. *An introduction to numerical analysis*. John Wiley & Sons, Inc, 1988.
- [2] E.F.F. Botta. *De Methode der Eindige Elementen*. Lecture notes, Department of Mathematics, RuG, 1991.
- [3] R. Jielof & A. Spoor & H. de Vries. The microphonic activity of the lateral line. *J. Physiol.*, 116:137–157, 1952.
- [4] E.J. Dijkstra. Pulsating entry-flow in a straight circular tube. Master's thesis, Department of Mathematics, RuG, 1991.
- [5] H.W. Hoogstraten. *Stromingsleer*. Lecture notes, Department of Mathematics, RuG, 1992.
- [6] M. Meeuwissen. Een numeriek model van de beweging van een cupula in een zijlijnkanaal. Master's thesis, Department of Mathematics, RuG, 1994.
- [7] G. Segal. *SEPRAN sepra analysis*. SEPRAN Handleiding, University of Delft, 1984.
- [8] P.T.S.K. Tsang. *Laser interferometric flow measurements in the lateral line organ*. PhD thesis, Department of Biophysics, RuG, 1997.
- [9] P.W.J. van Hengel. *Emissions from cochlear modelling*. PhD thesis, Department of Biophysics, RuG, 1996.
- [10] S.M. van Netten & A.B.A. Kroese. Laser interferometric measurements on the dynamic behaviour of the cupula in the fish lateral line. *Hearing Research*, 29:55–61, 1987.
- [11] S.M. van Netten. Hydrodynamics of the excitation of the cupula in the fish lateral line. *J. Acoust. Soc. Am.*, 89(1):310–319, 1991.
- [12] S.M. van Netten & S.M. Khanna. Stiffness changes of the cupula associated with the mechanics of hair cells in the fish lateral line. *Proc. Natl. Acad. Sci. (USA)*, 91(2):1549–1553, 1994.